

A Blade Element Momentum Method for  
Dynamic Analysis of Vertical Axis Wind  
Turbines - Rev B

Karl O. Merz  
NTNU, Department of Civil and Transport Engineering  
Trondheim, Norway

November 9, 2011

### **Abstract**

A computer program has been developed to calculate the aerodynamic loads on a vertical-axis wind turbine. The program is based upon a double-multiple streamtube blade element momentum method. The approach is unique in that it explicitly models many blades about the azimuth of the rotor; a number of fictitious (ghost) blades are modelled, in addition to the real blades. In this manner, the induced velocity is allowed to evolve naturally, according to a dynamic inflow model, while the flow about the blades is also allowed to evolve naturally, according to a dynamic stall model. The rotor therefore responds appropriately to the spatial and frequency distribution of fluctuations in the incoming velocity.



# Contents

<b>1</b>	<b>Introduction</b>	<b>7</b>
1.1	Coordinate Systems . . . . .	8
1.2	Problem Setup and Required Inputs . . . . .	10
1.2.1	Discretization of the Blade and Swept Surface . . . . .	11
1.2.2	Chord, Twist, and Pitch . . . . .	12
1.2.3	Blade Azimuth Angle . . . . .	12
1.2.4	Incoming Airflow . . . . .	14
<b>2</b>	<b>Airfoil Forces</b>	<b>15</b>
2.1	Airfoil Coefficients . . . . .	15
2.1.1	Airfoil Coefficient Extrapolation . . . . .	16
2.2	Dynamic Stall . . . . .	18
2.2.1	Separation Point Motion . . . . .	20
2.2.2	Implementation of the Øye Method . . . . .	20
2.2.3	Positive and Negative Angles-of-Attack . . . . .	22
2.2.4	An Example of Dynamic Stall . . . . .	23
2.2.5	Changes in Reynolds Number . . . . .	26
<b>3</b>	<b>Momentum Balance</b>	<b>31</b>
3.1	Momentum Balance Equation . . . . .	31
3.2	Double-Multiple Streamtube BEM . . . . .	32
3.3	Correction for Finite Aspect Ratio . . . . .	33
3.4	Induced Velocity . . . . .	34
3.5	Dynamic Inflow . . . . .	37
3.6	Vector Versus $X^r$ Momentum Balance . . . . .	38
<b>4</b>	<b>Validation</b>	<b>41</b>
<b>5</b>	<b>Conclusions</b>	<b>49</b>



# Revision Log

Rev A: Corrected an error in calculating the matching velocity, which was previously incorrectly set to the same value as the velocity upwind of the rotor. Updated the plots.

Rev B: Section 3.6 has been added. This section discusses momentum balance using the full three-component  $V_i$  induced velocity vector, in comparison with only the  $(V_i^r)_X$  component.

Using the full  $V_i$  vector, the matching velocity must also include all three components. This was implemented, and the plots in Chapter 4 have been updated according to the latest version of the software.

Deleted the placeholder chapter on turbulence; the turbulence model can be considered independently of the basic aerodynamic methods described in this document.



# Chapter 1

## Introduction

A computer program, implementing a double-multiple streamtube type of blade element momentum (BEM) method, has been developed for calculating aerodynamic loads on vertical-axis wind turbine (VAWT) blades. The program is intended for preliminary analyses, with the current motivation being to design the generator torque control system of a Darrieus turbine mounted atop a floating platform.

The blade element momentum method implemented here is not accurate enough to be recommended for final design or certification. More advanced methods are required in order to accurately predict power and loads above the rated windspeed. In particular, a more complex dynamic stall model is required. Also, the present approach does not explicitly represent the convection of flow through the interior of the turbine. These shortcomings are discussed further in Chapters 2 and 3.

Alternatives to the BEM method include wake vortex analysis or some form of CFD. In comparison with the BEM method, these latter approaches are more physically accurate, but are very slow, and can be numerically unstable.<sup>1</sup> In general, it can be said that the BEM method is useful, because it provides an approximate solution with minimal computational effort.

Under quasi-steady conditions, solution by the BEM method consists of iterating between local forces at the blades and the change in the momentum of the air that flows through the surface swept by the blades: these aspects of the analysis are discussed in Chapters 2 and 3, respectively. Under dynamic conditions, though, the calculation is not iterative. Rather, a time-delay function, described in Section 3.5, is applied which numerically damps the momentum calculation.<sup>2</sup> Provided that timesteps are small, the solution is numerically stable.

The present implementation of the BEM method is well-suited for calculating aerodynamic loads under atmospheric turbulence, as well as translational motion (as a rigid body) of the rotor.<sup>3</sup> Limitations in the BEM method – in particular, the lack of an explicit model of the wake as it is convected through the rotor – require the use of simplifying assumptions. The implementation of turbulence in the software can be considered independently from the basic

---

<sup>1</sup>For example, Leishman [12] p 95, discussing free-wake vortex methods

<sup>2</sup>This time-delay has a physical basis, as it represents the downwind convection of vorticity in the wake.

<sup>3</sup>... for example, a rotor on a floating wind turbine.



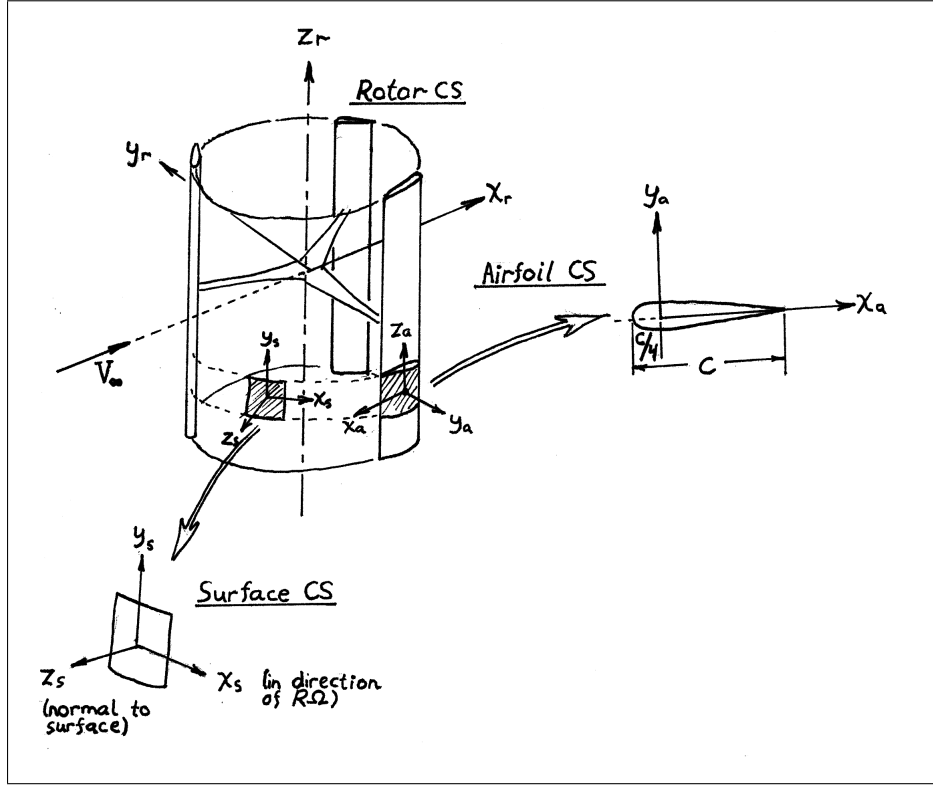


Figure 1.1: Definitions of coordinate systems

momentum-balance calculation. A discussion of turbulence is therefore deferred to a future document. (Reference [18] presents the results of an initial investigation.)

Chapter 4 compares output power calculated by the BEM code against measurements on a 17 m diameter turbine tested at Sandia Laboratories. There are clear shortcomings in the BEM method, but the predictions are good enough to be useful for tuning a generator torque control system, provided that some adaptability is built into the algorithm.<sup>4</sup>

## 1.1 Coordinate Systems

There are three coordinate systems which are relevant to the VAWT aerodynamic loads calculation. These are the rotor, airfoil, and surface coordinate systems, which are shown in Figure 1.1. (There are two other coordinate systems which are needed when turbulence and rotor translation are included in the model. These are a fixed global coordinate system, and the “wind” coordinate system, associated with the turbulent windfield.)

<sup>4</sup>In other words, the generator torque should not be decided based upon a fixed schedule, as a function of windspeed, derived from a BEM analysis. The algorithm should consider the measured rotational speed and power output and adapt the torque accordingly.

The rotor coordinate system has its origin at the geometric center of the rotor. The  $Z_r$  axis is aligned with the axis of rotation, and the  $X_r$  axis points in the mean downwind direction. Thus the  $(Y_r Z_r)$  plane defines the “upwind” and “downwind” halves of the rotor. The azimuth angle  $\psi$  is defined relative to the  $X_r$  axis.

According to the above definition, the rotor coordinate system shifts, relative to a ground-fixed coordinate system, with both the attitude of the turbine and the average direction of the incoming wind. This is necessary in order to define pairs of elements that form a streamtube, without making the calculations unduly complicated. In reality, as the rotor translates or the wind changes direction, the position of the rotor changes with respect to the existing vortex wake. This effect is not captured in the present analysis; it is implicitly assumed that the position of the rotor and the mean wind direction change over timescales that are greater than a couple rotor revolutions. Note, however, that changes in the *incoming* velocity (as opposed to the wake induced velocity) caused by motion of the rotor can be accounted for by modifying the input velocity field.

There is an airfoil coordinate system associated with each blade element. The origin of the airfoil coordinate system is located at the quarter-chord point. The  $X_a$  axis is opposite the direction of rotation, and the  $Y_a$  axis is perpendicular to the swept surface, when the blade pitch and twist angles, measured about the  $Z_r$  axis, are zero. The angle-of-attack  $\alpha$  is defined relative to the airfoil coordinate system.

Finally, there is a surface coordinate system associated with each swept surface element. (The swept surface is the surface formed by rotating the blade quarter-chord line  $360^\circ$  about the  $Z_r$  axis.) The  $Z_s$  axis is normal to the surface, pointing outwards, while the  $X_s$  axis points in the direction of rotation. The surface coordinate system is used in the momentum balance portion of the calculation.

It is required to refer vectors to one coordinate system or the other. This requires use of transformation matrices. The transform from the rotor to the airfoil coordinate system is defined in the following manner:

1. Define  $Z_a$  parallel to  $Z_r$ ,  $Y_a$  parallel to  $X_r$ , and  $X_a$  opposite  $Y_r$ :

$$T_1 = \begin{bmatrix} 0 & -1 & 0 \\ 1 & 0 & 0 \\ 0 & 0 & 1 \end{bmatrix}. \quad (1.1)$$

2. Rotate about the  $Z_r$  axis by the blade pitch angle  $\zeta$  plus twist angle  $\xi$ :

$$T_2 = \begin{bmatrix} \cos(\zeta + \xi) & \sin(\zeta + \xi) & 0 \\ -\sin(\zeta + \xi) & \cos(\zeta + \xi) & 0 \\ 0 & 0 & 1 \end{bmatrix}. \quad (1.2)$$

3. Rotate about the  $Y_r$  axis by the blade tilt angle  $\beta$  (Figure 1.2):

$$T_3 = \begin{bmatrix} \cos \beta & 0 & -\sin \beta \\ 0 & 1 & 0 \\ \sin \beta & 0 & \cos \beta \end{bmatrix}. \quad (1.3)$$

4. Rotate about the  $Z_r$  axis by the azimuth angle  $\psi$ :

$$T_4 = \begin{bmatrix} \cos \psi & \sin \psi & 0 \\ -\sin \psi & \cos \psi & 0 \\ 0 & 0 & 1 \end{bmatrix}. \quad (1.4)$$

5. Finally:

$$T_r^a = T_1 T_2 T_3 T_4, \quad \text{and} \quad T_r^r = (T_r^a)^{-1} = (T_r^a)^T. \quad (1.5)$$

Definition of the surface coordinate system is similar:

1. Define  $Y_s$  parallel to  $Z_r$ , and  $Z_s$  parallel to  $X_r$ :

$$T_1 = \begin{bmatrix} 0 & 1 & 0 \\ 0 & 0 & 1 \\ 1 & 0 & 0 \end{bmatrix}. \quad (1.6)$$

2. Rotate about the  $Z_r$  axis by the offset angle  $\eta$  (Figure 1.3):

$$T_2 = \begin{bmatrix} \cos \eta & \sin \eta & 0 \\ -\sin \eta & \cos \eta & 0 \\ 0 & 0 & 1 \end{bmatrix}. \quad (1.7)$$

3. Rotate about the  $Y_r$  axis by the blade tilt angle  $\beta$  (Figure 1.2):

$$T_3 = \begin{bmatrix} \cos \beta & 0 & -\sin \beta \\ 0 & 1 & 0 \\ \sin \beta & 0 & \cos \beta \end{bmatrix}. \quad (1.8)$$

4. Rotate about the  $Z_r$  axis by the azimuth angle  $\psi$ :

$$T_4 = \begin{bmatrix} \cos \psi & \sin \psi & 0 \\ -\sin \psi & \cos \psi & 0 \\ 0 & 0 & 1 \end{bmatrix}. \quad (1.9)$$

5. Finally:

$$T_r^s = T_1 T_2 T_3 T_4, \quad \text{and} \quad T_r^r = (T_r^s)^{-1} = (T_r^s)^T. \quad (1.10)$$

## 1.2 Problem Setup and Required Inputs

The following information is required as input to the BEM method:

1. the blade profile, in terms of  $(r, z)$  coordinates defining a discrete set of nodes in cylindrical polar coordinates; also, the tangential distance out of the  $(r, z)$  plane, if the blade is offset or swept like an airplane wing;
2. aerodynamic lift, drag, and moment coefficients  $C_L$ ,  $C_D$ , and  $C_M$  for each blade element, with properties being assumed constant between each set of nodes;

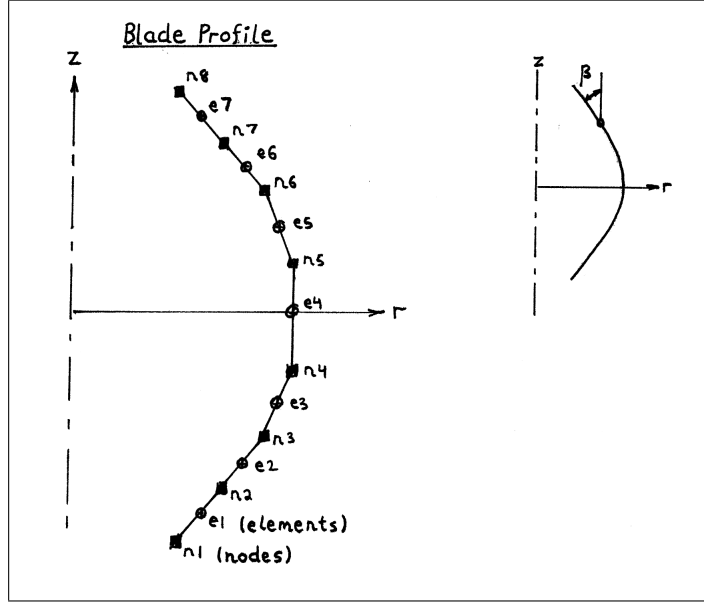


Figure 1.2: Blade profile definition

3. the chord length and static twist angle of each blade element, along with the pitch angle of the blade;
4. the number of blades and the azimuth angle of blade number one (the blades are assumed to be equally spaced);
5. the rotational speed;
6. the properties of the ambient air: density and viscosity; and,
7. the magnitude and direction of airflow incident upon each element of the upwind half of the swept surface; that is, at a particular location on the rotor, the velocity that the air would have if the rotor were not there.

### 1.2.1 Discretization of the Blade and Swept Surface

The blade is defined by a profile of nodes in cylindrical coordinates (Figure 1.2): distance from the axis of rotation  $r$ , distance along the axis of rotation  $z$ , and a tangential offset (Figure 1.3). Note that a tangential offset (“swept wing”) is equivalent, from the perspective of a blade element, to increasing the radius and modifying the blade pitch angle.

Blade elements are defined between adjacent nodes, interpolating separately the magnitude and direction of the vector coordinate of each node. The element’s normal vector is perpendicular to the line connecting its bounding nodes.

Figure 1.4 illustrates the discretized swept surface. To discretize the swept surface into surface elements, the blade profile is rotated at discrete intervals, interval  $k$  being at azimuth angle  $90^\circ + (\delta\psi)/2 + k \delta\psi$ . At each interval, the (rotated) blade element centroids and normal vectors define the surface element

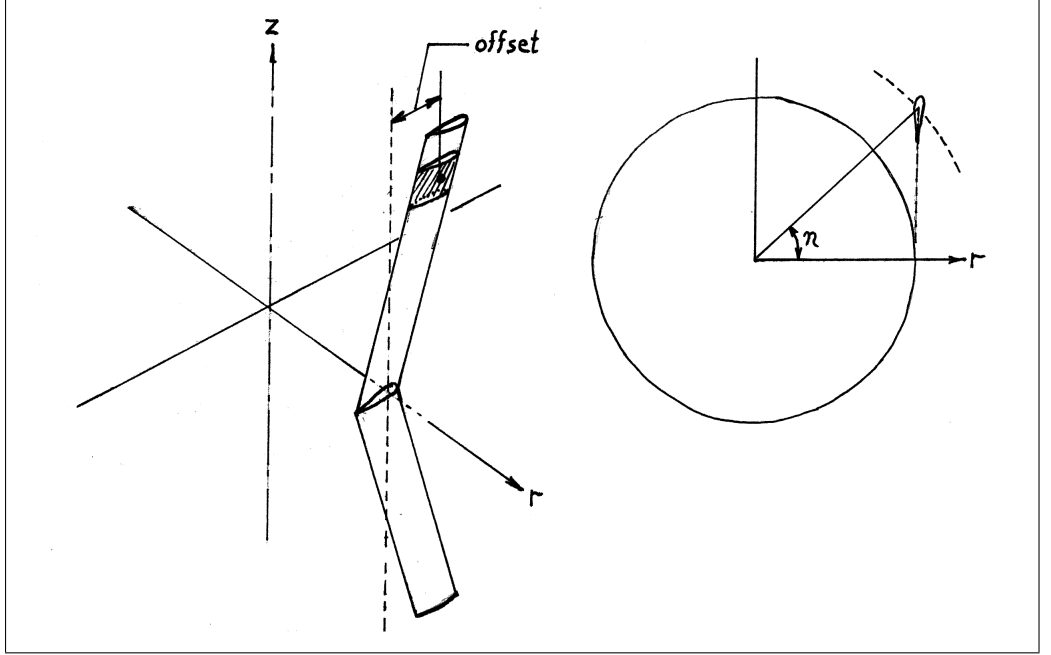


Figure 1.3: Offset of the blade profile to define a “swept-wing” configuration

centroids ( $x_s$ ) and normal vectors ( $n_s$ ). Thus, the length of each surface element is the same as its generating blade element. The width of each surface element is:

$$w_e = \delta\psi \sqrt{(x_s^r)_X^2 + (x_s^r)_Y^2}. \quad (1.11)$$

### 1.2.2 Chord, Twist, and Pitch

The chord of the blade,  $c$ , is defined as in Figure 1.1. Figure 1.5 illustrates twist and pitch angles. The twist angle of a blade element,  $\xi$ , is the rotation about the  $Z_a$  axis, relative to some fixed reference on the blade. The pitch angle of the blade,  $\zeta$ , is the rotation of all elements on the blade, about their  $Z_a$  axes. The algorithm that transforms coordinates should work for straight blades with twist and pitch control, or an arbitrary blade profile with twist, but not an arbitrary blade profile with pitch control, because the algorithm does not account for the translation of elements which are not aligned with the blade pitch axis.

### 1.2.3 Blade Azimuth Angle

For purposes of input, one of the blades is designated Blade #1, and an initial azimuth angle is given for this blade; Figure 1.6. The other blades are assumed to be evenly spaced about the azimuth.

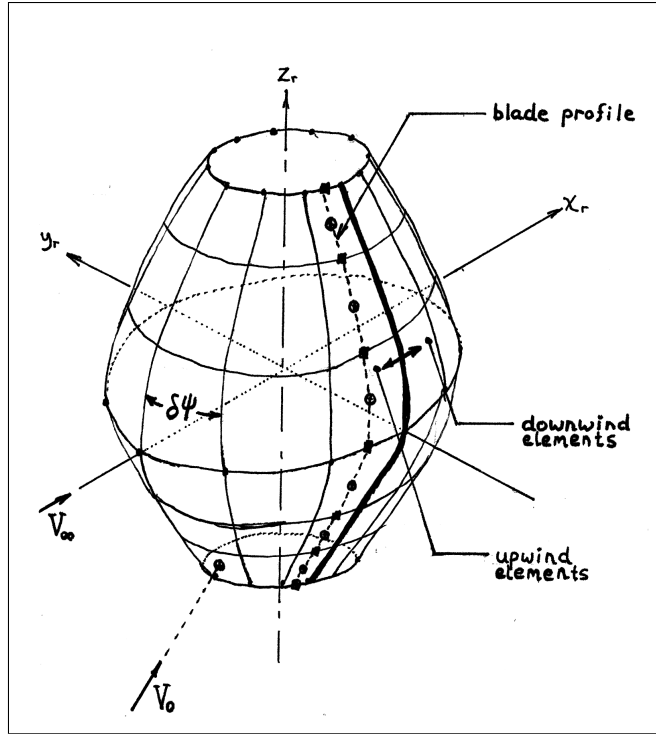


Figure 1.4: Discretization of the swept surface by rotating the blade profile

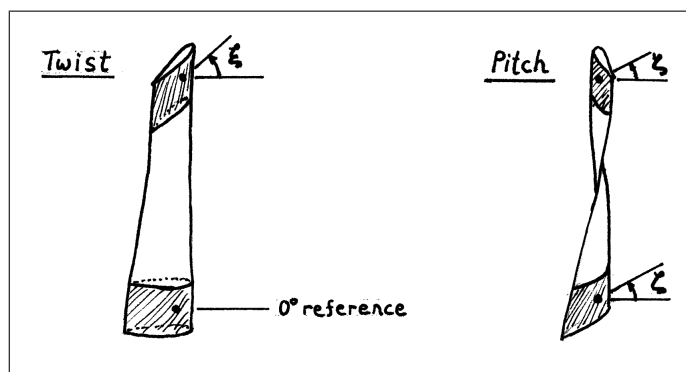


Figure 1.5: Blade twist and pitch angles

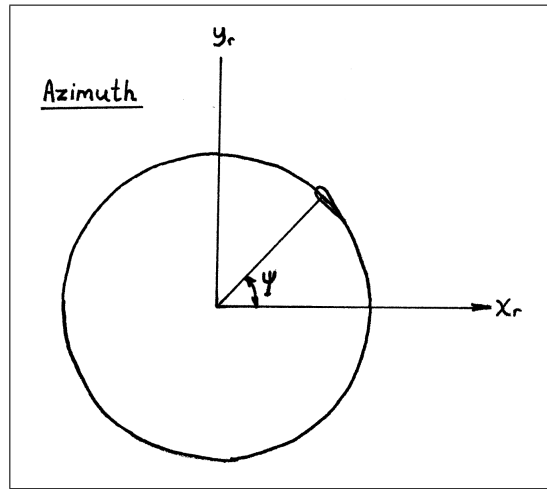


Figure 1.6: Azimuth angle

#### 1.2.4 Incoming Airflow

The incoming air velocity vector,  $V_0$ , must be given for each upwind surface element. An example is shown in Figure 1.4. The  $V_0$  vectors may vary in magnitude and direction, in order to model turbulence, however assumptions of the analysis will be violated if the direction of incoming flow diverges greatly from one surface element to another. That is, turbulence should be small fluctuations imposed on a uniform incoming flow.

## Chapter 2

# Airfoil Forces

Airfoil forces are computed by first looking up coefficients from an input table, as a function of Reynolds number  $Re$  and the instantaneous angle-of-attack  $\alpha$ , and then correcting the coefficients for dynamic stall.

Interpolating coefficients from the input table is the most computationally-intensive part of the BEM calculation. The calculation can be sped up significantly by modelling the coefficient curves with a series of closed-form equations, as functions of  $Re$  and  $\alpha$ .

### 2.1 Airfoil Coefficients

Induced velocity  $V_i^a$ , remote air velocity  $V_0^a$ , and blade velocity  $V_b^a$  are obtained in airfoil coordinates, transforming from rotorplane coordinates. Relative air velocity at the airfoil is calculated as:

$$V^a = V_0^a + V_i^a - V_b^a \quad (2.1)$$

Figure 2.1 shows an example of these velocity vectors. (Note that  $V_b$  in the sketch is drawn negative, opposite the velocity of blade motion.  $V_b$  should be input to the software as the positive velocity vector of blade motion.)

Here an approximation must be made. Airfoil coefficients are based upon test data in which there is no spanwise flow, perpendicular to the airfoil cross-section. In most cases, the flow about an actual wind turbine blade will have a spanwise component of velocity, especially with a Darrieus type turbine, portions of whose blades are not perpendicular to the wind. This spanwise velocity is neglected when computing airfoil loads. Define a velocity magnitude:

$$|V| = \sqrt{(V^a)_X^2 + (V^a)_Y^2} \quad (2.2)$$

where  $(V^a)_X$  is the  $X$  component and  $(V^a)_Y$  the  $Y$  component of relative air velocity in airfoil coordinates. Define the angle-of-attack:

$$\alpha = \tan^{-1} \left( \frac{(V^a)_Y}{(V^a)_X} \right) \quad (2.3)$$

Define Reynolds number:

$$Re = \frac{\rho |V| c}{\mu} \quad (2.4)$$



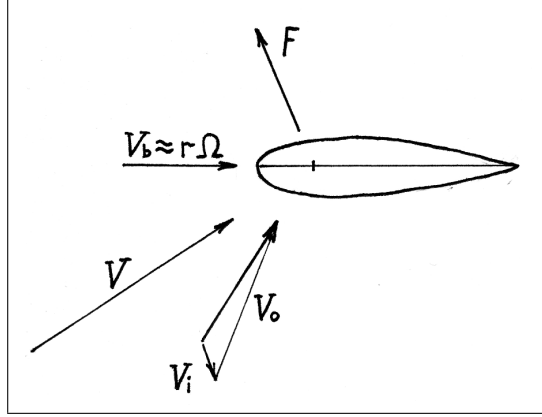


Figure 2.1: Velocity vectors that are components of the local velocity at the blade

where  $\rho$  is air density,  $\mu$  is air viscosity, and  $c$  is the airfoil chord length. Given Reynolds number and angle-of-attack, airfoil coefficients are calculated using linear interpolation between available tabulated values. Forces are computed from airfoil coefficients:

$$\begin{aligned} F_L &= \frac{1}{2} C_L \rho |V|^2 c L \\ F_D &= \frac{1}{2} C_D \rho |V|^2 c L \\ M &= \frac{1}{2} C_M \rho |V|^2 c^2 L \end{aligned} \tag{2.5}$$

Lift and drag forces are broken into their components in the airfoil coordinate system:<sup>1</sup>

$$\begin{aligned} (F_b^a)_X &= -F_L \sin \alpha + F_D \cos \alpha \\ (F_b^a)_Y &= F_L \cos \alpha + F_D \sin \alpha \\ (M_b^a)_Z &= M \end{aligned} \tag{2.6}$$

The Z component of moment results in torsion of the blade. This moment plays no role in the remainder of the momentum balance calculation, although it is included in the final loads output.

### 2.1.1 Airfoil Coefficient Extrapolation

Tabulated airfoil data rarely includes coefficients for angles-of-attack significantly beyond stall; for typical airfoils, stall occurs when the magnitude of angle-of-attack exceeds somewhere between  $10^\circ$  and  $20^\circ$ .<sup>2</sup> The blades of a VAWT will

<sup>1</sup>Drag and lift forces are by definition parallel to and perpendicular to the flow direction at the blade. The airfoil X and Y axes are parallel to and perpendicular to the chord of the airfoil. Drag and lift are offset from the airfoil X and Y axes by the angle-of-attack.

<sup>2</sup>Abbott and von Doenhoff [1] appendix IV

operate beyond stall over the downwind portion of rotation when windspeeds are high. Therefore, values for coefficients at high angles-of-attack must be estimated theoretically; a modified flat-plate theory is used.

To estimate lift and drag coefficients ( $C_L$  and  $C_D$ ) in the deep-stall range, first a matching point is defined as the last (highest angle-of-attack) data that the user has entered. Denote the matching point with a subscript  $s$ :  $C_{Ls}$ ,  $C_{Ds}$ , and  $\alpha_s$ .

The maximum drag, when the airfoil is oriented perpendicular to the flow ( $\alpha = \pm 90^\circ$ ), is calculated by:<sup>3</sup>

$$C_{D,\max} = 2 - 0.82 \left( 1 - e^{-17/\text{AR}} \right) \quad (2.7)$$

where AR is the aspect ratio of the entire blade, which can be computed by:<sup>4</sup>

$$\text{AR} = \frac{(R_o - R_i)^2}{\sum (c L)} \quad (2.8)$$

Then, lift and drag coefficients are extrapolated by the following formulas:<sup>5</sup>

$$C_L = \frac{C_{D,\max}}{2} \sin 2\alpha + (C_{Ls} - C_{D,\max} \sin \alpha_s \cos \alpha_s) \left( \frac{\sin \alpha_s}{\cos^2 \alpha_s} \right) \left( \frac{\cos^2 \alpha}{\sin \alpha} \right) \quad (2.9)$$

$$C_D = C_{D,\max} \sin^2 \alpha + \frac{C_{Ds} - C_{D,\max} \sin^2 \alpha_s}{\cos \alpha_s} \cos \alpha \quad (2.10)$$

Moment coefficient extrapolation is performed by the method of Lindenburg. [15] First, the airfoil, when oriented perpendicular to the flow, is represented by a wedge, as shown in Figure 2.2. Nose and tail wedge angles  $\phi_n$  and  $\phi_t$  are estimated by the user, and defined in the airfoil data file. Next, normal force coefficient is calculated by rotating lift and drag coefficients into rotorplane coordinates:

$$C_N = C_L \cos \alpha + C_D \sin \alpha \quad (2.11)$$

A semi-empirical expression is used to compute the location at which the resultant of the normal force acts. As a fraction of chord length, the expression is:<sup>6</sup>

$$x_{cp} = 0.5 - 0.35[\phi_t(0.2 + 0.08\phi_t) + (0.3 - \phi_n(0.2 + 0.08\phi_n))(1 - 1.8\sqrt{r_n/c}) - 0.3] \quad (2.12)$$

<sup>3</sup>Lindenburg [15], figure 2.4, plots several proposed expressions for the drag of a rectangular plate, orthogonal to the flow, as a function of the plate's aspect ratio. The expressions are all essentially in agreement with each other and with the test data. I used the one recommended by Lindenburg.

<sup>4</sup> $c$  and  $L$  are the chord and spanwise lengths of individual blade elements. The sum is taken over all the elements on the current blade.

<sup>5</sup>Moriarty and Hansen [19] p 22; watch out for the typo in equation 102.

<sup>6</sup>The expressions for  $x_{cp}$  and  $C_M$  were taken from Lindenburg [15], p 16.

where  $r_n$  is the nose radius, and  $c$  is the chord, as shown in Figure 2.2. Note that  $\phi_n$  and  $\phi_t$  should be in units of radians when used in the above equation (they are input by the user as degrees). Moment coefficient is calculated by:

$$C_M = -C_N \left[ x_{cp} - 0.16 \left( 1 - \frac{2\alpha}{\pi} \right) - 0.25 \right] \quad (2.13)$$

where  $\alpha$  is in radians.

## 2.2 Dynamic Stall

The aerodynamic pressure forces on an airfoil exhibit time-history effects; the forces at a given point in time are a function of both the instantaneous and previous flow conditions. In wind turbine analysis software, these time-history effects are typically referred to as dynamic stall; although time-history effects are present under all flow conditions, they are particularly pronounced in the vicinity of initial stall.

Dynamic stall behavior dominates the performance of a vertical-axis wind turbine above the rated windspeed. (Figures 4.2 and 4.8 show examples.) There is a large difference in the predicted power at high windspeeds, between analyses that omit and include dynamic stall.

Although the flow about a blade in stall is highly complex, simplified engineering methods have been shown to capture the most important effects. One example is the Leishman-Beddoes dynamic stall model,<sup>7</sup> which includes:

1. a time-delay associated with the change in circulation (lift) under attached-flow conditions;
2. a time-delay associated with the change in leading-edge pressure, which lags the circulation;
3. a time-delay associated with the movement of the separation point (the chordwise location on the airfoil at which flow separates from the low-pressure surface), which lags the leading-edge pressure; and,
4. a model of vortex shedding from the leading-edge, which tends to occur under large changes in angle-of-attack, and results in a sharp spike in the normal force.

An alternative, and much simpler, dynamic-stall model was presented by Øye [20]. This approach combines the first three time-delays into a single one, and omits leading-edge vortex shedding. Studies comparing dynamic stall models, such as Larsen et al. [11] and Paraschivoiu ([21], Section 6.5), indicate that the Leishman-Beddoes dynamic stall model is more accurate, but that the Øye model captures the most important effect, which is the delay in motion of the separation point.<sup>8</sup> In light of this, it was decided to implement the Øye model in the present version of the BEM software.

<sup>7</sup>Leishman and Beddoes [13],[14]

<sup>8</sup>The data presented by Gupta and Leishman [5] indicates that the “trigger” for leading-edge vortex shedding, defined in the Leishman-Beddoes model, does not always trip when it should. In other words, the Leishman-Beddoes model does not always properly account for leading-edge vortex shedding. Correcting this would require refinement of the criteria for initiation of vortex shedding.

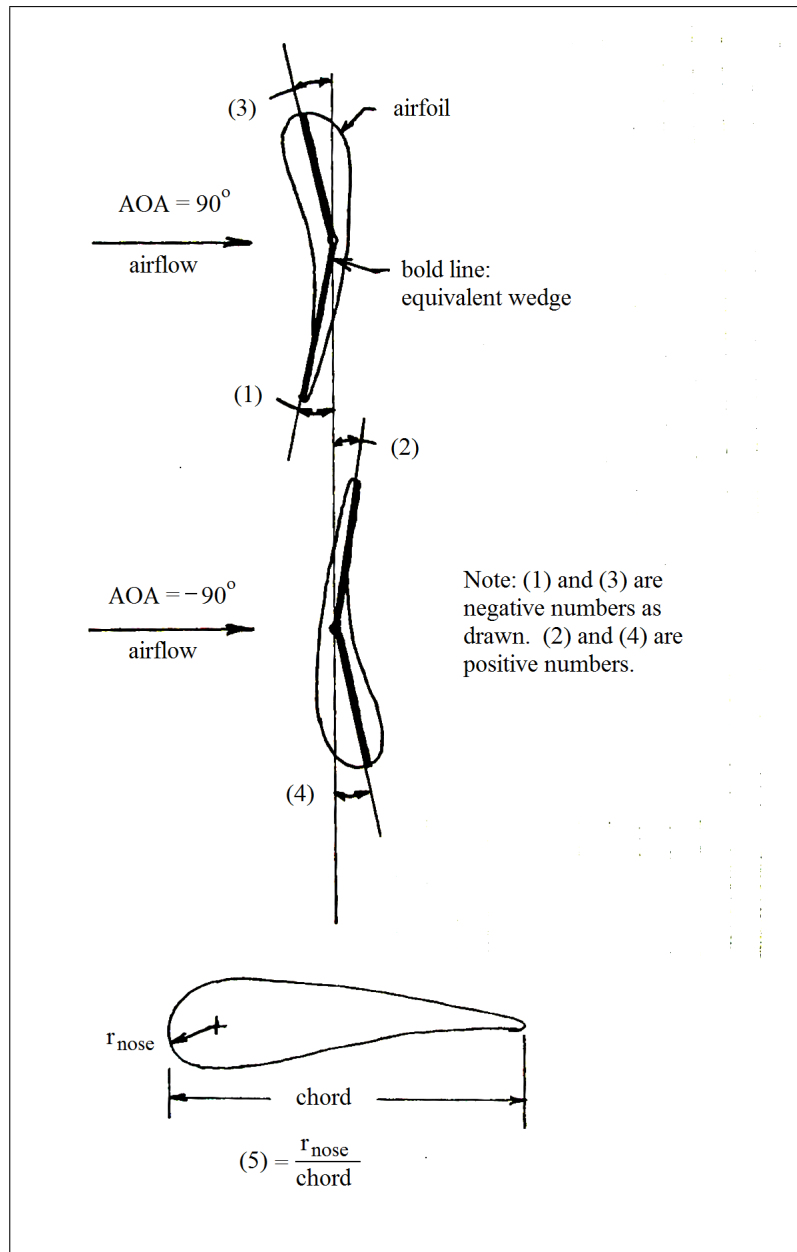


Figure 2.2: Definition of parameters used to extrapolate airfoil coefficients

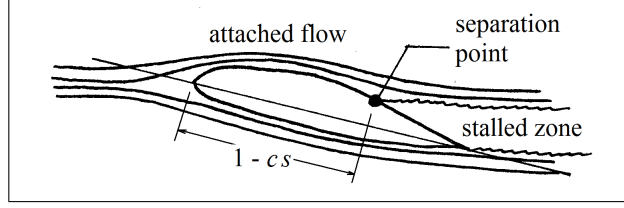


Figure 2.3: A parameterization of the location of the separation point along the low-pressure surface, in terms of the parameter  $s$

### 2.2.1 Separation Point Motion

The basic features of dynamic stall can be understood in terms of a time-delay on the motion of the separation point with respect to the instantaneous angle-of-attack. To express this mathematically, the position of the separation point along the low-pressure surface of the airfoil is parameterized by a variable  $s$ . The definition of  $s$  is sketched in Figure 2.3: it is the fraction of the chord length measured from the trailing edge to the point of flow separation. Positive angles-of-attack are associated with positive  $s$ , and negative angles-of-attack are associated with negative  $s$ . Thus  $s$  is zero when flow is fully-attached, +1 when flow is fully-separated due to a large positive  $\alpha$ , and -1 when flow is fully-separated due to a large negative  $\alpha$ .<sup>9</sup>

Following Hansen et al. [6], the instantaneous lift coefficient  $C_L$  can be related to  $s$  by the Kirchhoff formula:<sup>10</sup>

$$C_L = \frac{1}{4} \left( \frac{dC_L}{d\alpha} \right)_a (\alpha - \alpha_z) \left( 1 + \sqrt{1 - |s|} \right)^2. \quad (2.14)$$

Here,  $\alpha_z$  is the angle-of-attack at zero lift, and:<sup>11</sup>

$$\left( \frac{dC_L}{d\alpha} \right)_a = \max_{\alpha_q} \left[ \frac{C_{Lq}}{\alpha_q - \alpha_z} \right]; \quad (2.15)$$

Equation 2.14 is valid when  $|s| < 1$ . For  $|s| \geq 1$ , the quasi-steady coefficient curve applies.

### 2.2.2 Implementation of the Øye Method

The key equation of the Øye method states that the instantaneous position of the separation-point  $s$  lags the quasi-steady position  $s_q$  – that is,  $s_q$  would be the location of the separation-point if  $\alpha$  were held constant for a long time. The time-lag function is:

$$\frac{ds}{dt} = \frac{s_q - s}{\tau}. \quad (2.16)$$

<sup>9</sup>This is opposite the usual definition of the separation-point position, which is typically measured from the *leading* edge. Because here we are dealing with both positive and negative angles-of-attack, it is most convenient that the separation-point parameter be continuous across the trailing edge.

<sup>10</sup>Leishman and Beddoes relate the *normal* force to  $s$  using this expression. The distinction is not so important for small angles-of-attack. In the context of the Øye method, it has been shown (for instance Fuglsang [3]) that there is very little hysteresis in the drag force, thus it seems appropriate to limit the separation-point function to the lift force.

<sup>11</sup>This comes from Hansen et al. [6] pp 11-12.

This has the solution:

$$s(t) - s_q = [s(t_0) - s_q]e^{-(t-t_0)/\tau}. \quad (2.17)$$

The present method differs from the original Øye model [20] in two ways. First, the Kirchhoff formula, Equation 2.14, is used to relate the position of the separation point to the lift coefficient. (This is consistent with Hansen et al. [7]. Øye used interpolation between the lift coefficient under fully-attached flow and a simplified estimate of the lift coefficient under fully-separated flow.) Second, the separation point is allowed to travel along both the upper and lower sides of the airfoil, because the angle-of-attack on a VAWT blade may be positive or negative. Special logic is required to handle the transition between flow separation on the upper and lower surfaces; otherwise, unrealistically high forces are obtained. This logic is described in Section 2.2.3. Here we limit the discussion to fluctuations that do not change the sign of the angle-of-attack.

The modified Øye method requires, as input, tabulated  $C_{Lq}$  versus  $\alpha$  data. This is the standard quasi-steady lift coefficient data; but here it is necessary to mark it with a  $q$  subscript, since the instantaneous value of  $C_L$  deviates from the quasi-steady curve. Several quantities must be defined (or located by searching numerically) based upon the tabulated data. These are  $\alpha_z$  and  $(dC_L/d\alpha)_a$ , from above, and the angle-of-attack at which flow is fully separated,  $\alpha_{FS}$ . This latter quantity is calculated by setting  $s$  to 1 (or -1) in Equation 2.14:

$$\alpha_{FS} = \alpha_z + 4 \frac{C_{Lq}}{(dC_L/d\alpha)_a}, \quad (2.18)$$

where both  $C_{Lq}$  and  $\alpha_{FS}$  lie upon the quasi-steady curve.<sup>12</sup>

Here is how the dynamic stall calculation works for a single timestep. For a given, instantaneous angle-of-attack  $\alpha$  (here considering only positive values, to keep the discussion simple), the quasi-steady position of the separation point can be calculated from Equation 2.14:

$$s_q = \begin{cases} 1; & \alpha \geq \alpha_{FS} \\ 1 - \left( 2 \sqrt{\frac{C_{Lq}}{(dC_L/d\alpha)_a(\alpha - \alpha_z)}} - 1 \right)^2; & \alpha < \alpha_{FS} \end{cases} \quad (2.19)$$

Equation 2.17 can be written, using discrete timesteps:

$$s(t) = s_q + [s(t - \Delta t) - s_q] e^{-\Delta t/\tau_s}, \quad (2.20)$$

which can be evaluated numerically, using  $s$  from the previous timestep, and the value of  $s_q$  from Equation 2.19.<sup>13</sup>

Once the position of the separation point  $s$  is known, the instantaneous lift coefficient can be calculated from Equation 2.14. It should be emphasized that in Equation 2.14  $\alpha$  is the instantaneous angle-of-attack, and  $s$  is the instantaneous separation point position. Observe that Equation 2.14 has been applied multiple times, to solve for different quantities. This is consistent, though, because different values of lift coefficient, angle-of-attack, and separation point have been used each time.

<sup>12</sup> $C_{Lq}$  is positive when  $\alpha$  is positive, and negative when  $\alpha$  is negative.

<sup>13</sup>It is assumed that  $s_q$  changes over a timescale that is large in comparison with  $\Delta t$ . Since  $s_q$  is calculated based upon the instantaneous  $\alpha$ , this means that the timestep  $\Delta t$  must be fine enough to smoothly capture changes in  $\alpha$ .

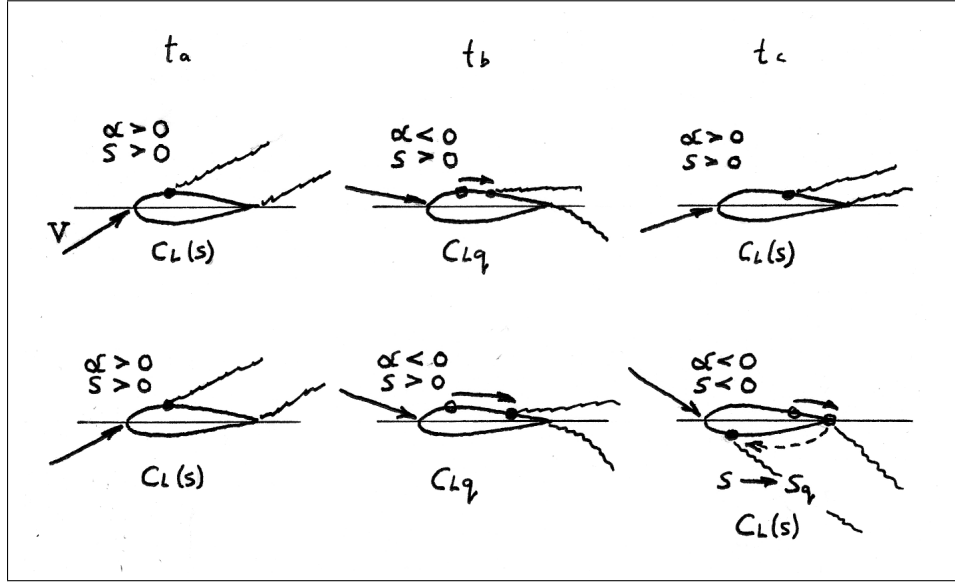


Figure 2.4: A sketch of two possible scenarios in which the sign of the angle-of-attack changes: in the first scenario, the sign changes only briefly, not long enough for the separation-point to reach the trailing edge on (what has now become) the high-pressure surface; in the second scenario, the sign changes for a longer length of time

### 2.2.3 Positive and Negative Angles-of-Attack

As a vertical-axis wind turbine rotates, the blade retreats from the wind over part of the cycle. When the windspeed is high, the angle-of-attack shifts rapidly from a large negative value to a large positive value, over a timescale that is comparable to  $\tau$ ; therefore dynamic stall is relevant.<sup>14</sup> However, the dynamic stall equations are not well-defined when  $\alpha$  and  $s$  are of opposite sign. Numerical studies showed that special logic is required to handle this situation.<sup>15</sup>

The logic is sketched in Figure 2.4, in this case for an angle-of-attack that begins positive and ends up negative. (The logic for an angle-of-attack that begins negative and ends up positive is the same, switching  $<$  and  $>$  signs.) The starting point, at time  $t_a$ , is a large positive  $\alpha$ , such that  $s$  is near 1. At time  $t_b$ , which is a very short time after  $t_a$ ,  $\alpha$  has rapidly decreased and become negative. Due to the time-lag (Equation 2.16),  $s$  remains on the upper (what has become the high-pressure) surface, although it begins to move towards the trailing edge.

The first question is: what should the value of the lift coefficient be at time  $t_b$ , when  $\alpha$  and  $s$  are of opposite sign? In reality, the state of flow about the airfoil will be complicated, and not easily represented by a simple force coefficient. It appears, though, that reasonable results are obtained if  $C_L$  is set to the quasi-

<sup>14</sup>Dynamic stall is also relevant on the upwind half of the rotation, but here the angle-of-attack is nicely behaved.

<sup>15</sup>Without special logic, it was observed that airfoil forces jumped instantaneously from one value to another; also, forces became unrealistically high when  $\alpha$  and  $s$  were of opposite sign.

steady value,  $C_{Lq}$ . For a retreating blade, in high winds,  $\alpha$  progresses from a large positive to large negative value; letting  $C_L = C_{Lq}$  results in a local power that is near zero, and a local thrust that points consistently downwind.

In some cases, in the immediate vicinity of  $\psi = 270^\circ$ , as the blade crosses from the upwind to downwind halves of the swept surface, and  $\alpha$  is near zero, it may switch signs several times, all in the span of a few timesteps.<sup>16</sup> This case is shown in the upper row of Figure 2.4. If, as in this example,  $\alpha$  fluctuates from positive to negative to positive again, with  $s$  remaining positive the entire time,<sup>17</sup> then at time  $t_c$  the lift coefficient should be calculated according to Equation 2.14. In other words, the calculation should proceed as if  $\alpha$  never changed sign.

The lower row in Figure 2.4 shows a more typical case, when  $\alpha$  retains its new sign. In reality, what will happen is that over some short period of time (a bit less than  $\tau$ ), the original circulation will be convected away, and circulation will build in the new direction, with flow separating from the new low-pressure surface, if  $\alpha$  is large enough. It was found that reasonable results are obtained if initially (at time  $t_b$ )  $C_L$  is allowed to attain its quasi-steady value  $C_{Lq}$ . Now, let  $t_c$  be the time at which the separation point (evolving according to Equation 2.17, as usual) reaches the trailing edge, and  $s$  switches sign. As it switches sign,  $s$  is made to “jump” to  $s_q$ , associated with  $\alpha$  and  $C_{Lq}$ . Then, during subsequent timesteps, the calculation proceeds as normal, according to Equations 2.14 and 2.17.

The above logic has the advantages that (1) there is no abrupt jump in the lift force as  $s$  “rounds the corner” at the trailing edge, even if  $\alpha$  varies wildly; and (2) the time-delay as  $s$  approaches the trailing edge has a physical basis, since, when  $\alpha$  abruptly changes sign, circulation and flow separation must build on the new low-pressure surface.

### 2.2.4 An Example of Dynamic Stall

The above dynamic stall calculations are illustrated here with an example. The VAWT BEM software was used to compute the aerodynamics of the Sandia 17 m diameter Darrieus VAWT, in its configuration with two NACA 0012 blades.<sup>18</sup> The turbine was set to rotate at a constant speed of 3.52 rad/s (33.6 rpm). The incoming wind was uniform and constant.

For a first analysis, the windspeed was set to 10 m/s. Figure 2.5 plots the angle-of-attack  $\alpha$ , separation-point position  $s$ , and contribution to the thrust  $(F^r)_X$  and torque  $T$  of a blade element adjacent to the equator of the turbine. (The blades were discretized into 20 elements along their length – corresponding to rows of the swept surface – thus Row 10 is just below the equator.) Here  $\psi$  is the azimuth angle, defined such that  $\psi = 0$  when the blade crosses from the downwind to the upwind side of the rotor (the  $Y^r$  axis).

The angle-of-attack varies through a range of approximately  $-20^\circ$  to  $+20^\circ$ , which means that the airfoil passes into and out of stall. This is evident from the separation-point position, which nears a magnitude of 1 (fully-separated flow) over both the upwind and downwind halves of the cycle.

<sup>16</sup>This has to do with the calculation of induced velocity.

<sup>17</sup>The logic given here is valid even if  $\alpha$  changes signs an unlimited number of times, as long as the sign of  $s$  stays the same.

<sup>18</sup>Chapter 4 provides references which contain a description of this turbine.



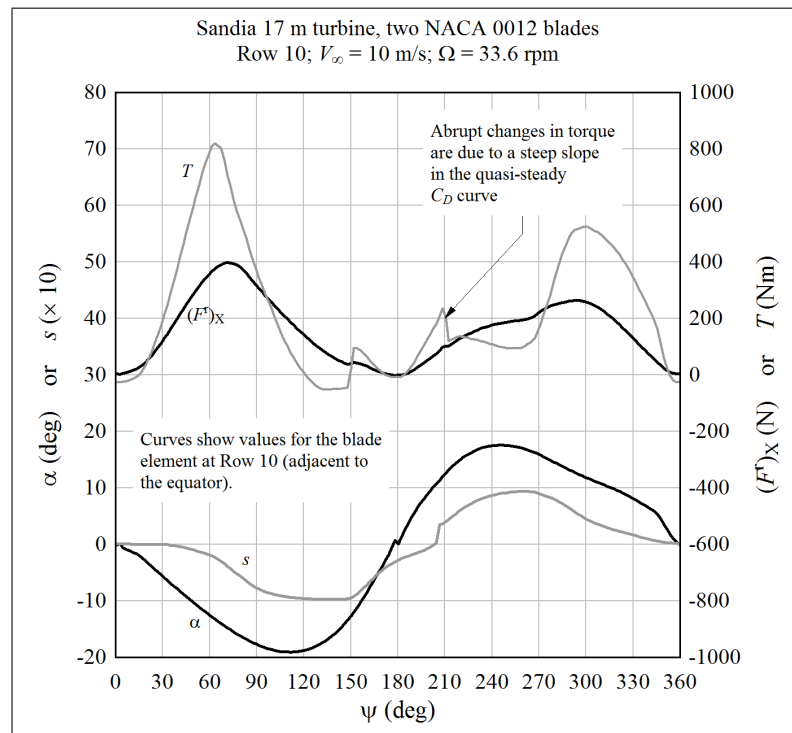


Figure 2.5: A plot of the aerodynamic state and forces at a location on the blade near the equator of the turbine, at a windspeed slightly over rated (for the chosen rotational speed)

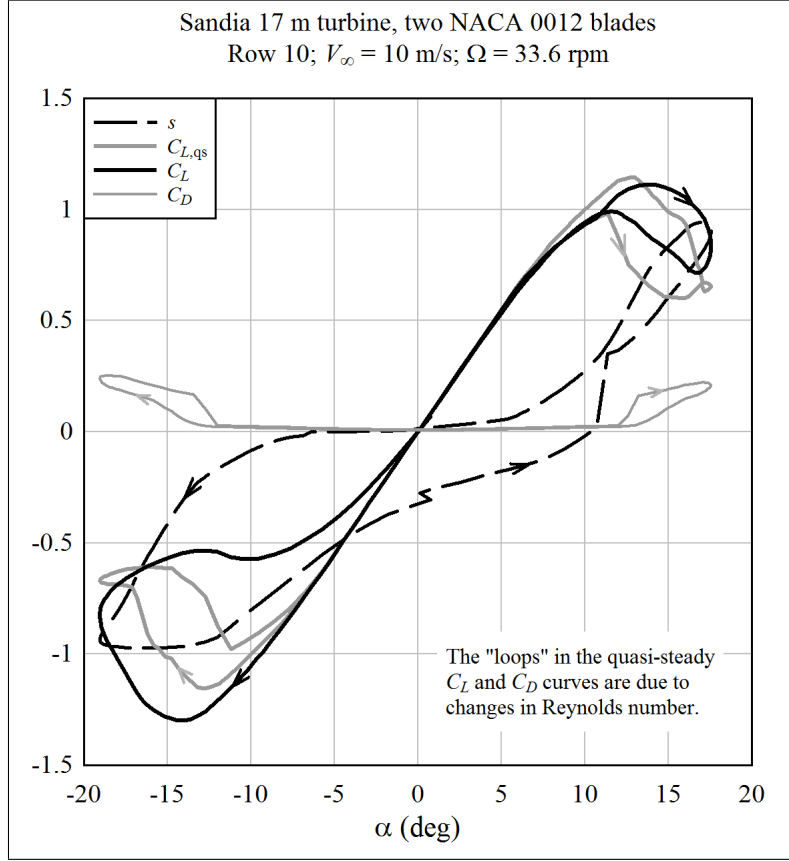


Figure 2.6: A plot of the aerodynamic state and forces at a location on the blade near the equator of the turbine, at a windspeed slightly over rated (for the chosen rotational speed), presented as airfoil coefficient curves

It is observed that there are sharp changes in the torque curve in the vicinity of  $\psi = 150^\circ$  and  $\psi = 210^\circ$ . These are artifacts of the quasi-steady drag coefficient curve,<sup>19</sup> which features an abrupt increase in drag at an angle-of-attack of about  $12^\circ$ ; thus the “jumps” in the torque are not related to the dynamic stall calculation.

At in azimuth  $\psi$  of about  $205^\circ$ , there is a jump in the separation-point position, from zero to its quasi-steady value. This is due to the logic shown in Figure 2.4, where the circulation about the airfoil is “recovering” from an abrupt change in the sign of the angle-of-attack, occurring at an azimuth of  $180^\circ$ . It can be seen from the thrust curve that the forces on the airfoil stay consistent as the separation-point position is reset.

Figure 2.6 provides an alternate view of the same blade element forces. Here the forces (expressed in the local airfoil coordinate system) are reduced to lift and drag coefficients, and are plotted against the instantaneous angle-of-attack.

The quasi-steady lift coefficient  $C_{L,qs}$  is plotted as a thick gray line. It is

<sup>19</sup>See Figure 2.6.

noteworthy that there is significant hysteresis in the quasi-steady curve; this is due to changes in the Reynolds number as the airfoil advances and retreats from the incoming wind. (The NACA 0012 airfoil is sensitive to the value of Reynolds number in the range  $5.6 \times 10^5$  to  $1.2 \times 10^6$ .)

The actual lift coefficient  $C_L$  is plotted as a thick black line. Starting with  $\psi = 0^\circ$ , at which  $\alpha \approx 0^\circ$ ,  $\alpha$  decreases, and a large dynamic-stall loop occurs as the airfoil sweeps over the upwind half of the rotor. As the airfoil retreats from the wind in the vicinity of  $\psi = 180^\circ$ ,  $\alpha$  rapidly changes sign. It can be seen that  $\alpha$  becomes positive while  $s$  is still negative. Here, the logic of Section 2.2.3 dictates that the lift coefficient should follow the quasi-steady value, which is indeed what is observed in Figure 2.6. After some time delay, over which circulation builds,  $s$  changes sign and jumps to its quasi-steady value. After this, the dynamic-stall calculation proceeds as normal, and a small hysteresis loop is observed as the airfoil sweeps over the downwind half of the rotor.

Abrupt changes in drag are evident in Figure 2.6; it is these which resulted in corresponding changes in torque, seen in Figure 2.5.

A second case was run, in which the windspeed was set to 20 m/s. Data was collected for a blade element at Row 16, which is midway between the equator and the root of the blade. Here the blade is slanted at an angle of about  $33^\circ$  with respect to the vertical.

Figures 2.7 and 2.8 show the angle-of-attack, separation-point position, and forces. In this case, the angle-of-attack cycles through  $360^\circ$  as the rotor rotates. Torque is produced over the half-cycle where the blade advances into the wind: the angle-of-attack crosses zero, so flow briefly attaches. (Attached flow can be identified by values of  $s$  near zero, in Figure 2.7 in the range  $0^\circ \leq \psi \leq 45^\circ$ .)

Figure 2.8 shows the airfoil forces, plotted as coefficient curves, in the vicinity of the region of attached flow. The angle-of-attack progresses from positive to negative – right to left, in Figure 2.8 – as the rotor spins. Due to the time-delay on flow attachment, the airfoil does not achieve its full quasi-steady lift coefficient when  $\alpha$  is positive; but then there is a pronounced dynamic-stall response when  $\alpha$  is negative.

When the blade is retreating from the wind, the flow comes from behind the blade, passing across the trailing edge. This is the reason for the jump from  $\alpha = -180^\circ$  to  $180^\circ$  seen in Figure 2.7. Here the airfoil coefficients are equal to their quasi-steady values.

It is seen that the dynamic stall logic of Section 2.2.3 results in smooth and continuous variations in forces over the entire angle-of-attack range.

### 2.2.5 Changes in Reynolds Number

The lift coefficient curve varies with the Reynolds number, and the Reynolds number varies with the local flow velocity. Therefore, to be precise, the dynamic stall parameters  $\alpha_z$ ,  $\alpha_{FS}$ , and  $(dC_L/d\alpha)_a$  should be derived from the coefficient tables during every timestep. This is computationally intensive. It is noted, however, that the coefficient curves are only weakly dependent upon the Reynolds number. Therefore, in the software, the parameters  $\alpha_z$ ,  $\alpha_{FS}$ , and  $(dC_L/d\alpha)_a$  are determined upfront, based upon a Reynolds number calculated

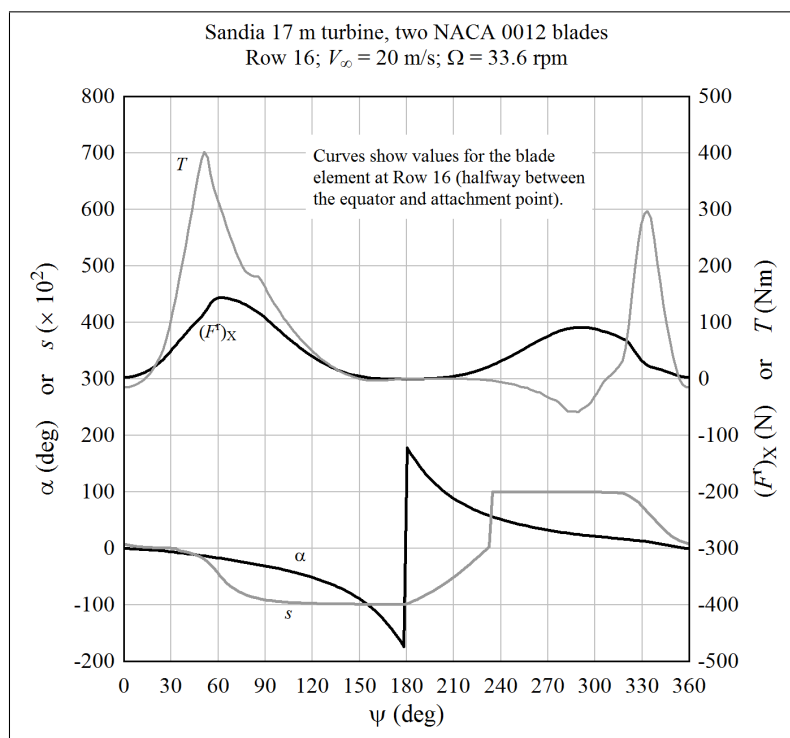


Figure 2.7: A plot of the aerodynamic state and forces at a location on the blade near the root of the blade, at a high windspeed

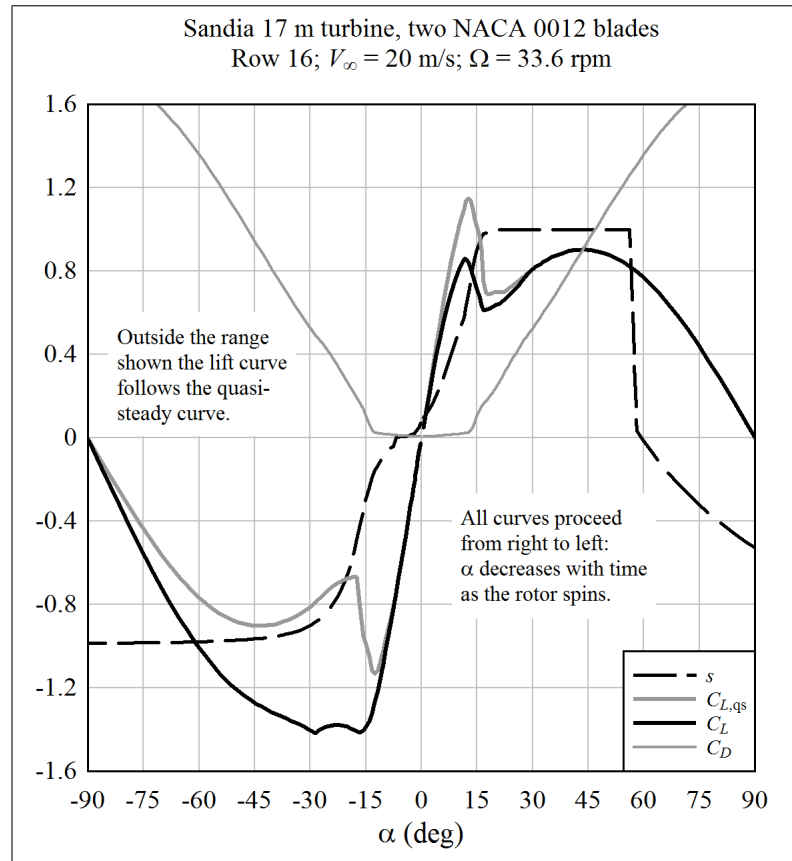


Figure 2.8: A plot of the aerodynamic state and forces at a location on the blade near the root of the blade, at a high windspeed, presented as airfoil coefficient curves

using a nominal local velocity:<sup>20</sup>

$$V = \sqrt{(r\Omega)^2 + V_\infty^2}, \quad (2.21)$$

with  $r = \sqrt{(x_b^r)_X^2 + (x_b^r)_Y^2}$ , where  $x_b^r$  is the position of the blade element centroid, in rotor coordinates.

---

<sup>20</sup>In the software, a block of code is included which, when un-commented, updates these parameters on each timestep; but then the calculation runs less than half as fast.



## Chapter 3

# Momentum Balance

The purpose of the momentum balance portion of the calculation is to find the induced velocity at the swept surface. The induced velocity is the change in velocity from far upstream to a location on the swept surface. In other words, the incoming velocity seen by the blade is  $V_0 + V_i$ , with  $V_0$  the remote velocity vector and  $V_i$  the induced velocity vector. Once  $V_i$  is known, the local velocity vector at the blade can be calculated as  $V = V_0 + V_i - V_b$  (where  $V_b$  is due to the motion of the blade). Then the forces along the blade can be calculated by the methods of Chapter 2.

Strictly speaking, the induced velocity is due to vorticity in the wake, which is well-defined only under conditions of attached flow. The flow through the rotor becomes more complicated when the blades stall. Nonetheless, the BEM method is applied at high windspeeds, with results that are accurate enough for a preliminary calculation.

### 3.1 Momentum Balance Equation

The vector momentum balance equation is:<sup>1</sup>

$$F = -2\rho A_e f |(V_0 + fV_i) \cdot n| V_i. \quad (3.1)$$

Here,  $F$  is the time-average force at the swept surface,<sup>2</sup>  $\rho$  is the air density,  $A_e$  is the area of the element of the swept surface, and  $f$  is the Prandtl factor. The term  $|(V_0 + fV_i) \cdot n|$  is the rate of flow through the surface element.

$F$  and the rightmost  $V_i$  (outside the absolute value sign) can in principle be expressed in any coordinate system; and the terms in the mass flow rate,  $|(V_0 + fV_i) \cdot n|$ , can also be expressed in any coordinate system. However, when dynamic inflow is considered (Section 3.5) it is most convenient to express momentum balance in the surface coordinate system:

$$F^s = -2\rho A_e f |(V_0^s)_Z + f(V_i^s)_Z| V_i^s, \quad (3.2)$$

---

<sup>1</sup>For example, Wilson and Lissaman [25], Burton et al. [2], and Hansen [7]. Reference [16] contains a derivation which uses the same terminology as this report.

<sup>2</sup>The time-average force is discussed further in Section 3.4. It represents the force of the air on the blades, rather than the blades on the air; hence the negative sign on the right-hand side of the equation.



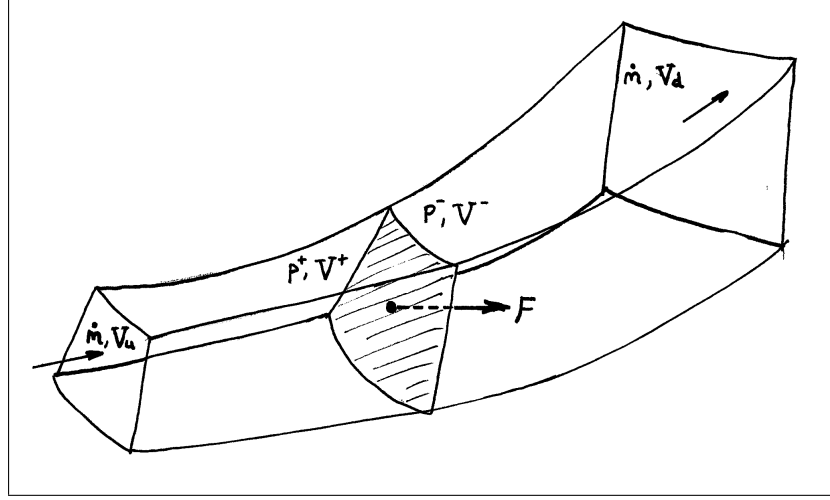


Figure 3.1: A streamtube passing through an element on the swept surface, at which a force is applied; the mass flow rate is conserved in the streamtube, as no flow passes through its walls

where only  $Z^s$  components are present in the mass flow rate term, which follows from the definition of the surface coordinate system (Figure 1.1).

Momentum balance applies to a streamtube passing through a fictitious surface in space, at which a force is applied. Such a streamtube is sketched in Figure 3.1. (The variables shown on the sketch are relevant for a detailed derivation of the momentum balance equation, and are not central to the discussion here.) For the concept of a streamtube to be valid, no flow can pass through its walls. This criterion is violated if  $(V_i^s)_Z > -0.5(V_0^s)_Z$ , because in this case the downstream flow reverses back towards the surface element. The only way this is possible, while preserving the conservation of mass, is for flow to cross the walls of the streamtube. In such a case, the actual physics of the flow would be complicated; but it can be said for certain that (for an energy extraction device) Equation 3.1 does not apply outside the range  $0 < (V_i^s)_Z < -0.5(V_0^s)_Z$ .<sup>3</sup> In the software,  $(V_i^s)_Z$  is limited to this range.

As discussed in Section 3.6, a similar constraint is applied to the components  $(V_i^s)_X$  and  $(V_i^s)_Y$ , in order to explicitly prohibit that the blades accelerate the flow.

### 3.2 Double-Multiple Streamtube BEM

For vertical-axis wind turbines, the BEM method is implemented as a “double-multiple streamtube” calculation. What this means is illustrated in Figure 3.2. Each swept surface element on the upwind side is associated with its mirror element across the  $(Y_r, Z_r)$  plane. It is assumed that the flow which leaves the

<sup>3</sup>As a technicality, note that this statement applies for the upwind half of the rotor. Because of the definition of the surface coordinate system, with the normal pointing outwards, the criterion is  $0 > (V_i^s)_Z > -0.5(V_0^s)_Z$  on the downwind half.

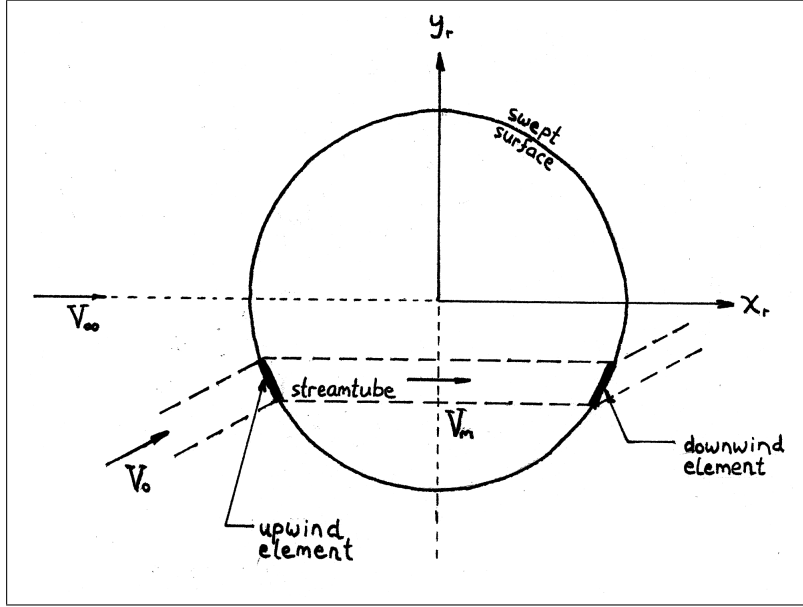


Figure 3.2: Double-multiple streamtube

upwind element subsequently impinges on the downwind element. Expansion and deflection of the airflow coming off the upwind half of the rotor are therefore neglected. The flow velocity “far” downstream of the upwind half is  $V_m = V_0 + 2V_i$ . This “matching” velocity  $V_m$  is used as the input to an identical set of calculations on the downwind surface element;  $V_m$  for the downwind element is akin to  $V_0$  for the upwind element.

### 3.3 Correction for Finite Aspect Ratio

The lift on a blade or wing of finite span goes smoothly to zero at the tips. However the tabulated airfoil data is derived from experiments which approximate an infinite span. Therefore the value of  $F_b$  must be modified.

Prandtl [22] developed a simple modification factor that is valid for tip-speed ratios above 5. (At tip speed ratios below 5, the Prandtl factor tends to overpredict the lift force.) The formula is:

$$f = \frac{2}{\pi} \cos^{-1} \left( e^{N_b(r-R)/(2r \sin \phi)} \right), \quad (3.3)$$

with:

$$\sin \phi = \frac{|V \cdot n|}{|V|}. \quad (3.4)$$

The vector  $V$  is the flow at the swept surface, including the remote velocity, the induced velocity, and the motion of the blade.

The wake of a straight-bladed (H-rotor) vertical-axis wind turbine is similar to the wake geometry analyzed by Prandtl. It can thus be argued that the

Prandtl factor should apply to a straight-bladed VAWT. For a Darrieus turbine, it is expected that the aspect ratio correction is negligible, with  $f \approx 1$  over the central portion of the blade that produces the majority of the power.

It was found that the solution could be numerically unstable at the elements adjacent to the blade root (very near the axis of rotation) if the Prandtl factor was applied to a Darrieus turbine. Therefore, while the software can calculate the Prandtl factor, it is recommended to set the factor to 1 when analyzing a Darrieus rotor. The Prandtl factor should be activated when analyzing an H-rotor.

### 3.4 Induced Velocity

It is not entirely obvious how to calculate the induced velocity over the rotor of a vertical-axis wind turbine, using momentum balance.<sup>4</sup> There are two things that make the calculation challenging: first, at a given element on the swept surface, a blade is present only a fraction of the time.<sup>5</sup> Second, because of dynamic stall effects, the blade arrives at the surface element with a state of flow that depends upon what the blade experienced during previous timesteps. Therefore the forces at a given surface element cannot be considered independent of the other surface elements.<sup>6</sup>

Because of these difficulties, there is no consensus on how the induced velocity should be calculated. Several options are presented in the literature.

The simplest option that is shown to give reasonable predictions of *average* power output is the method described by Paraschivoiu.<sup>7</sup> Here the induced velocity is considered to be constant over the upwind and downwind halves of the swept surface, not a function of the azimuth. In other words, the swept surface is divided into horizontal (constant latitude) bands, with each band being swept by a given spanwise element on the blade. Then the blade forces are integrated over the upwind and downwind halves of rotation. These average forces are used to find the average  $X^r$  component of induction,  $(\overline{V_i^r})_X$ , over the upwind and downwind halves of the band.

Paraschivoiu demonstrates that this sort of simplified calculation can be used to predict the global behavior of the rotor, although omitting the local variations in induced velocity tends to result in a moderate overprediction of power.<sup>8</sup> Another downside to taking an azimuth-average of the induction is that the instantaneous loads on the blade are not correctly predicted.<sup>9</sup> Thus if one is concerned with blade structural dynamics or fluctuations in power output, a more refined model is required.

---

<sup>4</sup>The theory is more straightforward if the wake is explicitly modelled, although in this case the calculations become much more complicated.

<sup>5</sup>Contrast this with a horizontal-axis wind turbine, where the swept surface is defined as an annulus swept by a spanwise section of the blades. In this case, the blades are always “present” at the swept surface.

<sup>6</sup>Again, contrast this with a horizontal-axis wind turbine, where it is typically assumed that each annulus is entirely independent of the others.

<sup>7</sup>Paraschivoiu [21], Section 6.4, describing the CARDAA software. Paraschivoiu later shows results from the CARDAAV software, which implements a local calculation of induced velocity, akin to the method used in this study.

<sup>8</sup>For instance, Paraschivoiu [21] Figure 6.35.

<sup>9</sup>Paraschivoiu [21] Figure 6.39

Homicz [8] studied the behavior of a VAWT under atmospheric turbulence, which required knowing the azimuthal variation of induced velocity. Therefore the swept surface was divided both horizontally and vertically into a series of approximately rectangular elements. Instead of taking an azimuthal average of blade forces, Homicz computed the time-average force at each surface element. For a rotor rotating at constant speed, this is equivalent to applying a factor of  $N_b \Delta\psi/2\pi$  to the local blade forces; in other words, the blade forces are factored by the fraction of the time that they spend at a given surface element, and this reduced force is used in Equation 3.1 to calculate the induced velocity.

Homicz made a simplifying assumption in order to decrease the calculation time: the induced velocity was calculated once, based upon steady flow conditions, at the beginning of the calculation. Then, it was assumed that the stochastic turbulence did not affect the induced velocity; in other words, the induced velocity was held constant<sup>10</sup> for the remainder of the analysis.

The assumption that induced velocity is constant in time is expected to be accurate if the velocity fluctuations due to turbulence are small in comparison with the mean velocity, if the frequency band of the turbulence is above the rotor rotational frequency  $\Omega/2\pi$ , and if  $\Omega$  is constant. These conditions may be satisfied in certain circumstances. However, the focus of the present project is a variable-speed VAWT. Also, when one looks at plots of windspeed under typical atmospheric conditions, it is seen that the windspeed can depart significantly from the average over a timescale of several tens of seconds. Therefore, it should not be assumed in general that the induced velocity is constant in time.

(That being said, it is also incorrect to assume that the induced velocity follows the local windspeed at each timestep, according to a quasi-steady, iterative solution of Equation 3.1. Rather, the induced velocity changes with the timescale of wake development, typically on the order of the period of one rotor revolution. This time-lag is implemented with a dynamic inflow model, as described in Section 3.5.<sup>11</sup>)

The question remains, then, how to calculate the appropriate force at each surface element, for use in Equation 3.1. There are two options. One option is to pretend that there is *always*, at each timestep, a blade associated with each surface element. In other words, the momentum balance calculation is performed for each surface element, independently of the actual azimuthal locations of the blades.<sup>12</sup> The problem with this approach is that the effects of dynamic stall must then be extrapolated from the previous *element*, rather than the previous *timestep*. In other words, the effective timestep for the dynamic stall analysis becomes a function of the number of elements that are used, rather than the physical timestep. This is undesirable.

<sup>10</sup>That is, constant in time. The induced velocity was calculated separately for each surface element.

<sup>11</sup>In typical implementations of the BEM method for HAWTs, dynamic inflow is not very important for stall-regulated turbines. The reason is that it is typical to calculate an average induction about the annulus swept by a given blade element. This area is spread over a large region of space, so high-frequency components of turbulence are not correlated, and tend to average to zero. The low-frequency components of turbulence, which are correlated over large distances, affect the induction in a quasi-steady manner. The situation is different for a VAWT, where one is looking at a small element on the swept surface. The induced velocity at such an element should not follow the high-frequency components of turbulence, therefore it is important to implement a time-lag.

<sup>12</sup>The calculated airfoil coefficients are factored by  $N_b \Delta\psi/2\pi$ , to provide the appropriate magnitude.

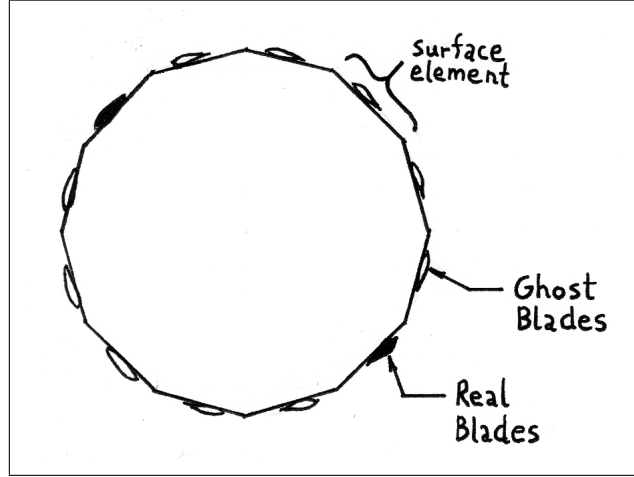


Figure 3.3: An illustration of ghost blades for a single row of elements about the rotor azimuth; the number of elements has been reduced for convenience of sketching ( $N_c = 36$  has been used in the analyses in this report)

The second option is to track the instantaneous blade forces as the blade sweeps across each surface element, and update the force term in the momentum balance equation only for those elements “containing” one of the blades. In this way, the dynamic stall calculation evolves naturally from one timestep to the next. The problem with this approach is that it tends to be numerically unstable, because the force associated with each element is updated in bursts. Also, it fits poorly with a dynamic inflow model.

A viable solution was found by combining the above two options. The aerodynamic model of the rotor is defined with  $N_c$  blades, where  $N_c$  is the number of columns into which the azimuth of the rotor is divided; that is,  $N_c = 2\pi/\Delta\psi$ . There are therefore  $N_b$  real blades, and  $N_c - N_b$  “ghost” blades, as sketched in Figure 3.3. In this manner, there is always the equivalent of one blade associated with each surface element. As the calculation proceeds, the state of flow about each blade, including dynamic stall, is allowed to evolve freely. The force associated with each surface element, for use in Equation 3.1, is taken as an average of the forces at the two adjacent blades, weighted linearly according to the distance of each blade from the element centroid, and factored by  $N_b/N_c$ .

Using ghost blades allows the induced velocity at each surface element to evolve naturally according to the dynamic inflow model, while at the same time the aerodynamic forces are allowed to evolve naturally according to the dynamic stall model. The calculation remains valid in the presence of turbulence and during changes in the rotational speed.

In the event that structural calculations are being performed, it is sufficient to limit aeroelastic analysis to the real blades, and consider the ghost blades to be perfectly rigid.

The downside of the ghost blade calculation is that it is slow, particularly when it comes to interpolating airfoil coefficients at each timestep for each blade. For a quick, approximate analysis, it is recommended to revert to the method

of Homicz: run a ghost blade analysis until induced velocities converge (roughly one revolution, if the dynamic inflow method of Section 3.5 is used), then freeze the induced velocities and consider only the real blades for the remainder of the analysis.

Note that induced velocities can be neglected when checking extreme gust loads, because at high windspeeds  $V_i$  is small with respect to  $V_0$ .

### 3.5 Dynamic Inflow

At each timestep, Equation 3.1 is solved in the following manner:

$$V_i = \frac{-F}{2\rho A_e f |(V_0^s)_Z + f(V_i^s)_Z|}, \quad (3.5)$$

where  $(V_i^s)_Z$  is taken to be the value at the previous timestep. (It is typically initialized to zero for the first timestep.) There are a couple issues with Equation 3.5, though. First, if iterated directly (including the necessary updating of  $F$  and  $f$ ), it tends to be numerically unstable. Second, the induced velocity is caused by vorticity in the wake, and therefore evolves on the same timescale as the wake, typically on the order of the period of one rotor revolution.

A dynamic inflow analysis addresses both these problems. A time-lag is introduced such that the induced velocity changes with the appropriate timescale. This introduces sufficient numerical damping so that the calculation is always stable.<sup>13</sup>

It does not appear, based upon a literature review, that a simple engineering-type dynamic inflow model has been developed specifically for VAWTs.<sup>14</sup> Therefore a model developed for HAWTs has been borrowed: the T.U. Denmark (TUDk) model described in Snel and Schepers [24]. In principle, the timescale of evolution of vorticity in the wakes of a HAWT and VAWT should be similar, therefore it is expected that the model is applicable, if not precise.

The TUDk model consists of two time lags in series:

$$v' + \tau_1 \frac{dv'}{dt} = v_q + 0.6\tau_1 \frac{dv_q}{dt}; \quad (3.6)$$

$$v + \tau_2 \frac{dv}{dt} = v'. \quad (3.7)$$

Here  $v_q$  is the quasi-steady induced velocity:  $V_i$  calculated according to Equation 3.5, using the instantaneous force at the surface element.  $v'$  is an intermediate variable, and  $v$  is the output, time-delayed induced velocity, that is used in the calculations of blade forces in the next timestep.

The time constants have been derived based upon horizontal-axis wind turbines. The first time constant is:

$$\tau_1 = \frac{1.1}{1 - 1.3a} \left( \frac{R}{|V_0|} \right), \quad (3.8)$$

where:

$$a = \frac{|V_i|}{|V_0|}. \quad (3.9)$$

<sup>13</sup>... unless one uses a ridiculously large timestep.

<sup>14</sup>Wake vortex and CFD models implicitly include the relevant physics.

For purposes of VAWT analysis,  $R$  is taken to be the outer radius of the rotor. The second time constant is:

$$\tau_2 = \left[ 0.39 - 0.26 \left( \frac{r}{R} \right)^2 \right] \tau_1. \quad (3.10)$$

Since, for a VAWT,  $r/R$  is poorly defined in this context, it is simply set equal to 0.7 to represent a “typical” value. Thus:

$$\tau_2 = 0.263\tau_1. \quad (3.11)$$

### 3.6 Vector Versus $X^r$ Momentum Balance

References describing the double-multiple streamtube BEM method, such as Paraschivoiu [21], consider only the  $X^r$  component of induced velocity  $(V_i^r)_X$ . In general, the conservation of momentum (Newton’s law) applies to each component of a vector: acceleration is aligned with the direction of force. In the case of a VAWT streamtube, the force at the airfoil includes axial, horizontal, and vertical components, and by Equation 3.1 it is expected that the direction of induced velocity opposes that of the force.

The BEM method does not indicate how the streamtubes evolve as they pass through the interior of the rotor. As stated in Section 3.2, it is assumed that the streamtubes pass directly through the rotor, aligned with the mean wind direction.<sup>15</sup> It would be expected that  $Y^r$  and  $Z^r$  components of induced velocity would change the direction of the streamtubes. Therefore, there are physical inconsistencies with the DMST BEM method, whether momentum balance is performed considering only the  $X^r$  component, or all three vector components, of induced velocity.

Two versions of the present software were created, one performing full vector momentum balance, and the other including only  $(V_i^r)_X$ , setting  $(V_i^r)_Y = (V_i^r)_Z = 0$ . Comparing output of the two versions, it was observed that differences in global, mean rotor loads were small: Figure 3.4 is typical. However, local airfoil forces may be different, especially away from the equator. Figures 3.5 shows an example of local blade thrust  $(F^r)_X$  and torque (tangential force times distance from the rotor axis) at a location near the equator, and Figure 3.6 shows the same quantities at a location away from the equator. The net effect of including transverse components of induced velocity is to transfer a portion of the energy extraction from the upwind to the downwind side of the rotor.

Working in the surface coordinate system, it is not entirely clear from the basic momentum theory what constraints should be placed on the  $X^s$  and  $Y^s$  components of induced velocity. Here it was decided to use the same type of constraint as for the  $Z^s$  component; that is,  $0 < (V_i^s)_X < -0.5(V_0^s)_X$  and  $0 < (V_i^s)_Y < -0.5(V_0^s)_Y$ . In this way, no component of the incoming flow is allowed to reverse, nor accelerate, downstream of the rotor.

Full vector momentum balance has been adopted as the default. It is suspected that this may provide a more accurate estimate of induced velocity when

<sup>15</sup>Paraschivoiu [21], pp 189-199, provides a method that can be used to estimate expansion of the streamtubes as they pass through the rotor, although only the  $X^r$  component of induced velocity is considered in the formulation. Modelling streamtube expansion in this manner does not have a significant effect on calculated blade loads.

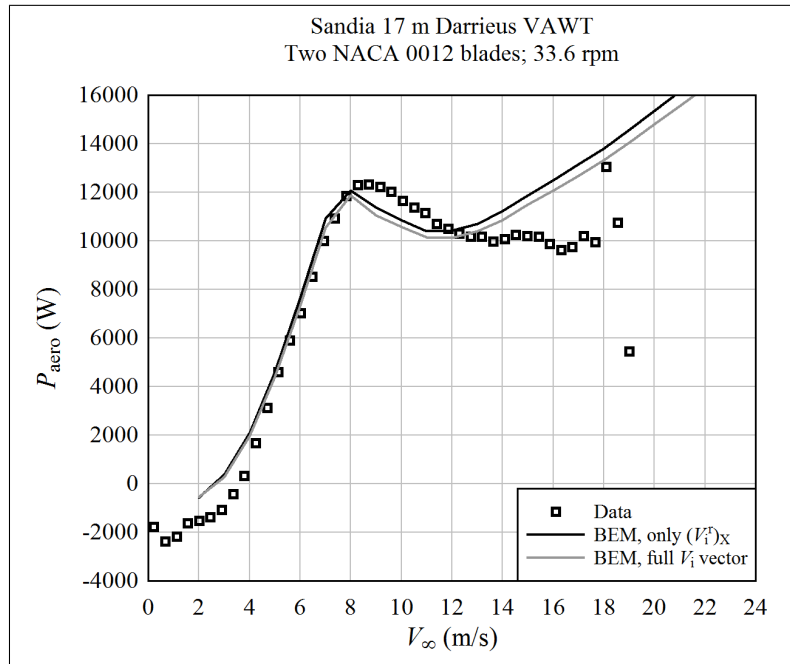


Figure 3.4:

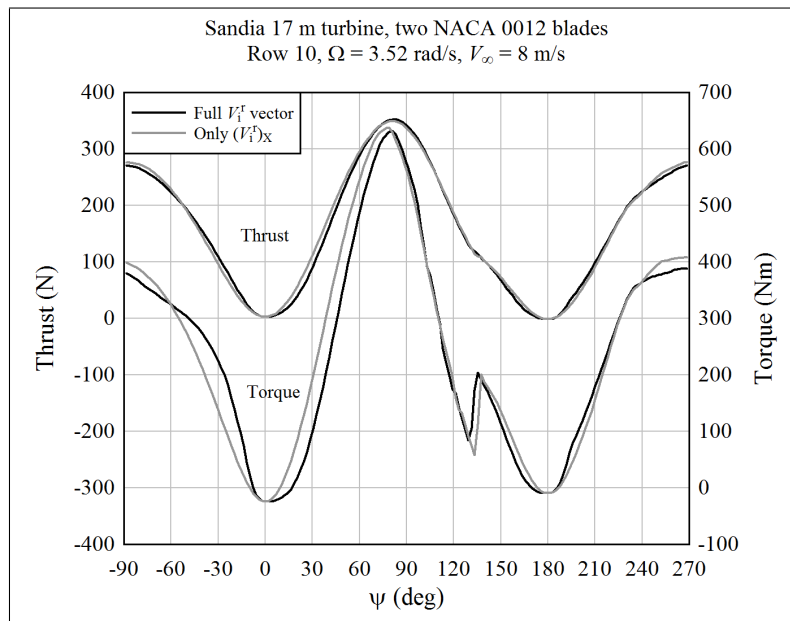


Figure 3.5:



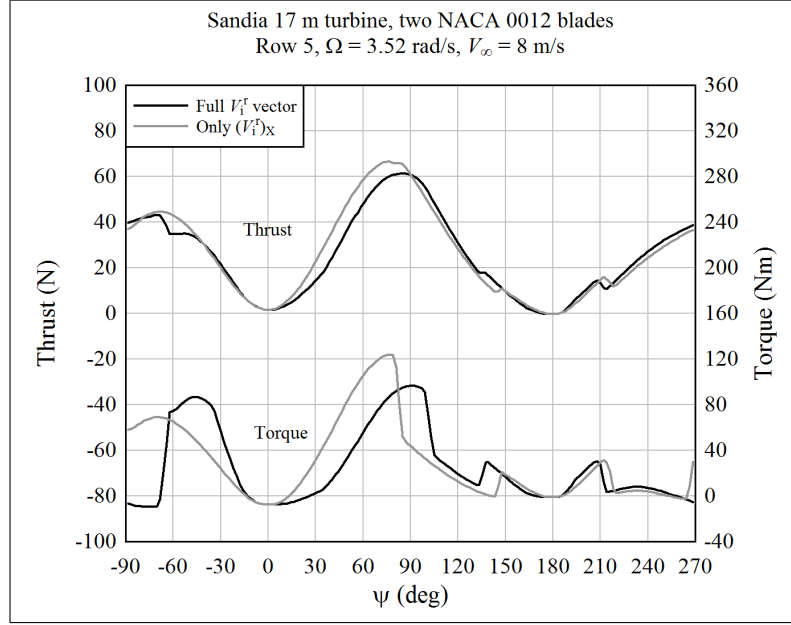


Figure 3.6:

flow over part of the rotor departs from the mean wind direction, as in a turbulent wind field. It may also give a more accurate estimate of induced velocity when the rotor is tilted (there is an incoming flow component along the  $Z^r$  axis). However, there is a lack of data which can be used to substantiate this.

## Chapter 4

# Validation

Operating data has been published for a number of VAWTs.<sup>1</sup> Among the published results, however, it is difficult to find a complete description that allows reproduction of the measurements. In particular, it is especially hard to find reliable airfoil coefficient data, at the appropriate Reynolds numbers.

The behavior of a VAWT at and above the rated power is very sensitive to the stall behavior of the airfoils. In other words, the behavior of the airfoil as the angle-of-attack approaches and exceeds the value at the maximum lift coefficient determines the behavior of the VAWT at high windspeeds.

Unfortunately, the lift and drag behavior beyond the maximum lift coefficient has traditionally been omitted from published airfoil datasets.<sup>2</sup> The data in this range was measured,<sup>3</sup> but not reported; it was not of interest to aircraft designers. In addition, symmetric airfoils, as used on VAWTs, have not been studied as extensively as cambered airfoils, as used on HAWTs or airplane wings.

As a result, the validation here is limited to one turbine, the Sandia 17 m diameter research prototype, tested in the late 1970's and early 1980's. The geometry of this turbine and measurements of the output power are described by Worstell.<sup>4</sup> The NACA 0012 airfoil was used for the blades; coefficients, including the critical range of stall, are provided by Sheldahl.<sup>5</sup> Although lift curves were reported up to  $Re = 1.76 \times 10^6$ , deep-stall drag coefficients were reported only up to  $Re = 7 \times 10^5$ . (It is not known why Sheldahl did not give the full drag curves for  $Re = 1.76 \times 10^6$ .) Therefore the trends seen at  $Re = 7 \times 10^5$  had to be extrapolated to higher Reynolds numbers.<sup>6</sup> Figure 4.1 shows the lift and drag coefficients that were used in the validation analyses.

Figures 4.2 through 4.8 compare the measured and calculated power curves of the Sandia 17 m turbine. First, focus on the attached-flow range, below the

---

<sup>1</sup>Paraschivoiu [21], Chapter 7, provides an overview of laboratory experiments and prototypes through the year 2002.

<sup>2</sup>For example, Abbott and von Doenhoff [1].

<sup>3</sup>Early NACA reports, like Goett and Bullivant [4], give full lift and drag data. But in these early tests there were errors in the drag measurement. [10]

<sup>4</sup>Worstell ([26] and [27])

<sup>5</sup>Sheldahl [23]. Only the experimentally-measured coefficients reported by Sheldahl should be trusted. Analytically-derived coefficients are also reported, but these contain errors in the lift and drag trends in the stalled range.

<sup>6</sup>Abbott and von Doenhoff [1] was used for the lift curve at  $Re = 3 \times 10^6$ , but drag data was not available past the point of maximum lift.

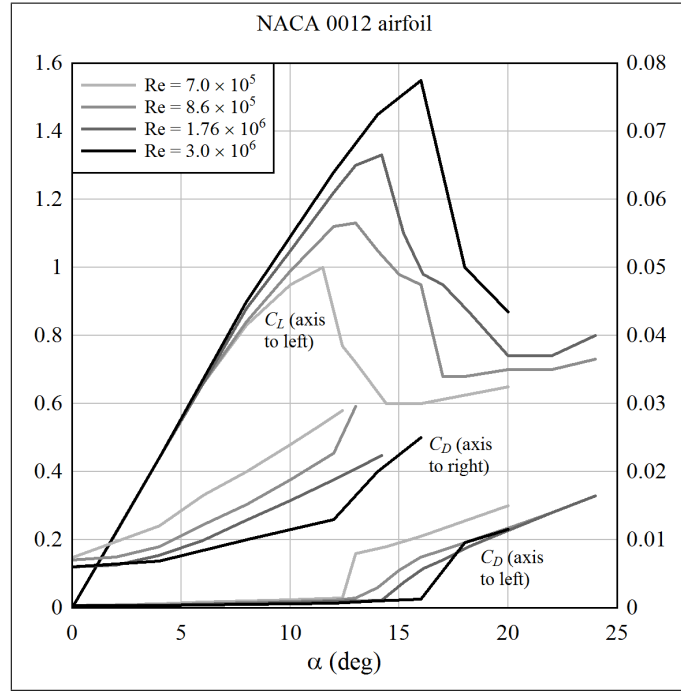


Figure 4.1: Estimated coefficients for the NACA 0012 airfoil

rated windspeed.<sup>7</sup> It is seen that, in this range, the trend in output power is well-predicted at low rotational speeds, and moderately overpredicted at high rotational speeds.

Below the rated windspeed, airfoil lift and drag data was available, and dynamic stall is not an issue. That the predictions of power are reasonably accurate in this range indicate that the implementation of the double-multiple streamtube momentum balance calculation is correct.

Above the rated windspeed, the behavior of a VAWT is very sensitive to the properties of the airfoils in stall, as well as the dynamic stall model. As described in the sections above, the coefficients are somewhat uncertain in the stalled range, and the dynamic stall model is one of the simplest available. Therefore, it is not surprising that the calculations do not precisely match the data. It is suspected, based upon a study by Paraschivoiu [21], that the underprediction of power is due primarily to the overly simple dynamic stall model, which does not consider phenomena such as leading-edge vortex shedding. That being said, the Øye dynamic stall model provides a large improvement over quasi-steady coefficients. This can be seen in the plots at 29.6 and 52.5 rpm, which include analyses with and without dynamic stall.

Figure 4.9 and 4.10 show power curves for the same turbine, but with three blades instead of two. The results are similar to those from the two-bladed case.

As another verification check, the power and thrust curves of the Deepwind 5 MW preliminary design, described in an informal document, was analyzed. The

<sup>7</sup>The rated windspeed can be taken as the windspeed at which the calculated power is maximum.

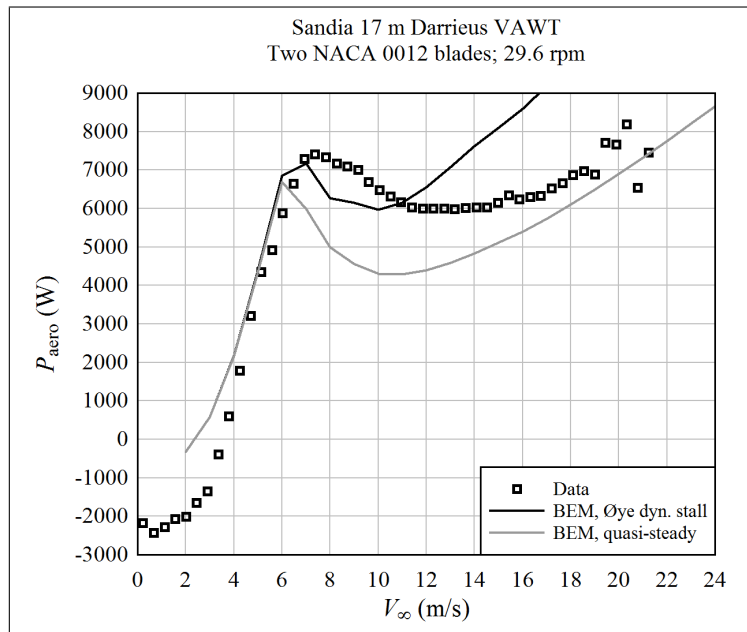


Figure 4.2: Aerodynamic power versus windspeed for the Sandia 17 m diameter turbine; two NACA 0012 blades; 29.6 rpm

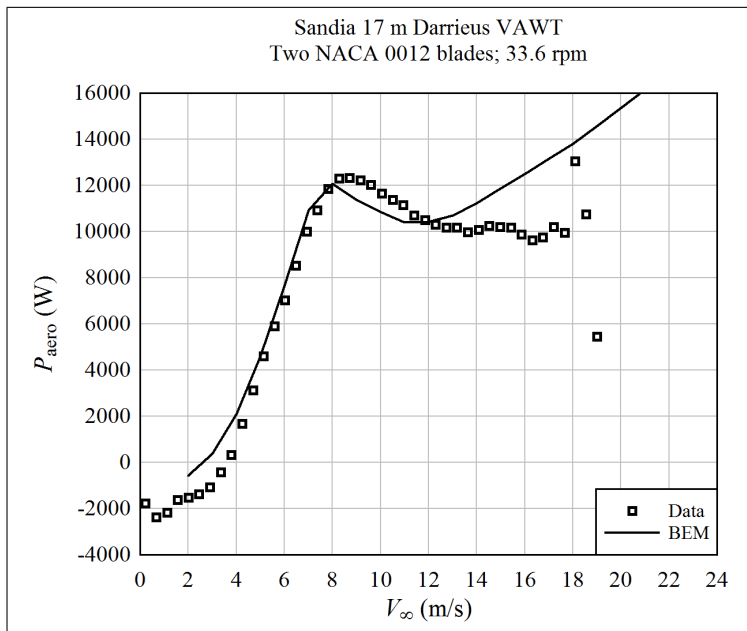


Figure 4.3: Aerodynamic power versus windspeed for the Sandia 17 m diameter turbine; two NACA 0012 blades; 33.6 rpm

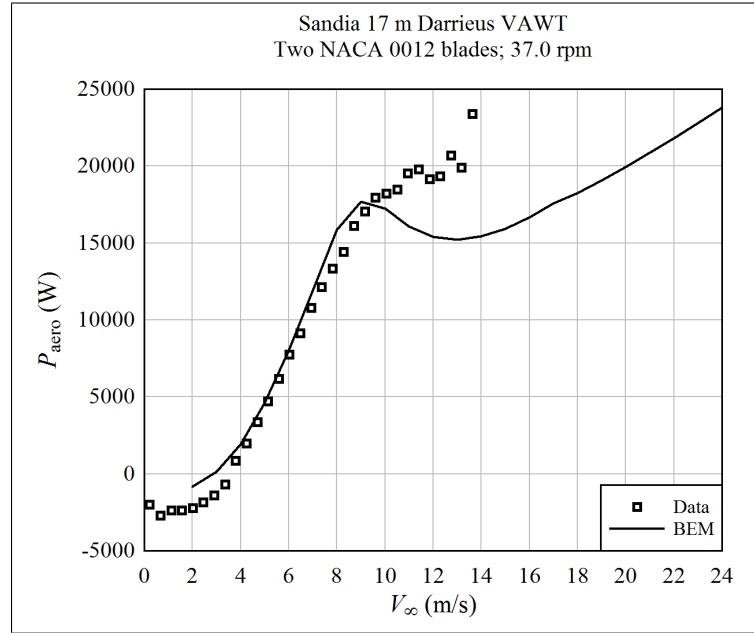


Figure 4.4: Aerodynamic power versus windspeed for the Sandia 17 m diameter turbine; two NACA 0012 blades; 37.0 rpm

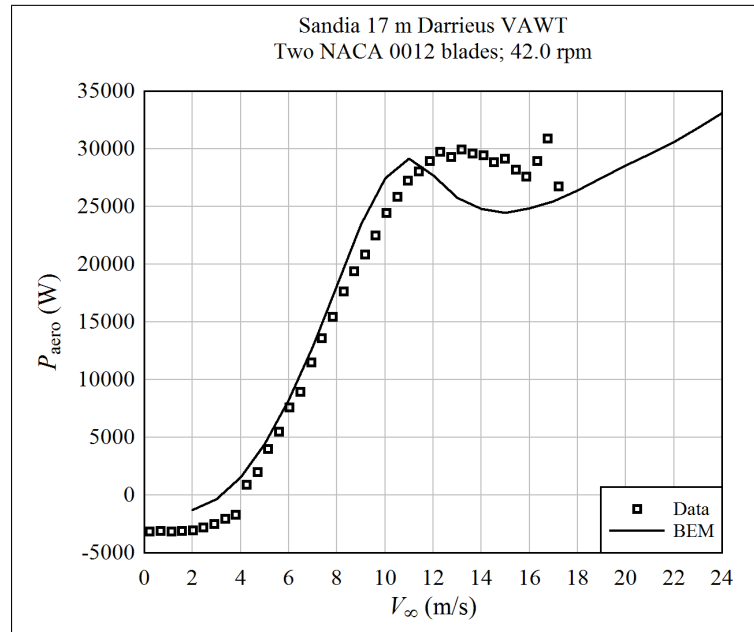


Figure 4.5: Aerodynamic power versus windspeed for the Sandia 17 m diameter turbine; two NACA 0012 blades; 42.0 rpm

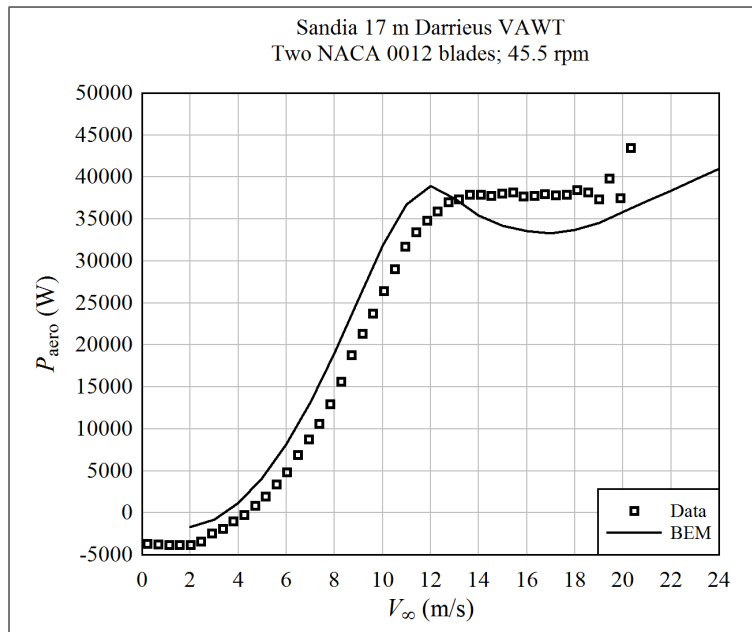


Figure 4.6: Aerodynamic power versus windspeed for the Sandia 17 m diameter turbine; two NACA 0012 blades; 45.5 rpm

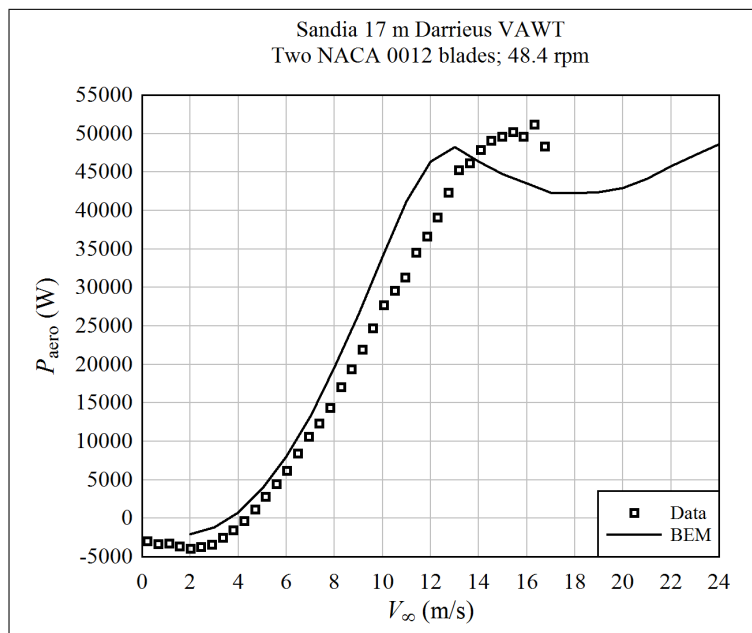


Figure 4.7: Aerodynamic power versus windspeed for the Sandia 17 m diameter turbine; two NACA 0012 blades; 48.4 rpm

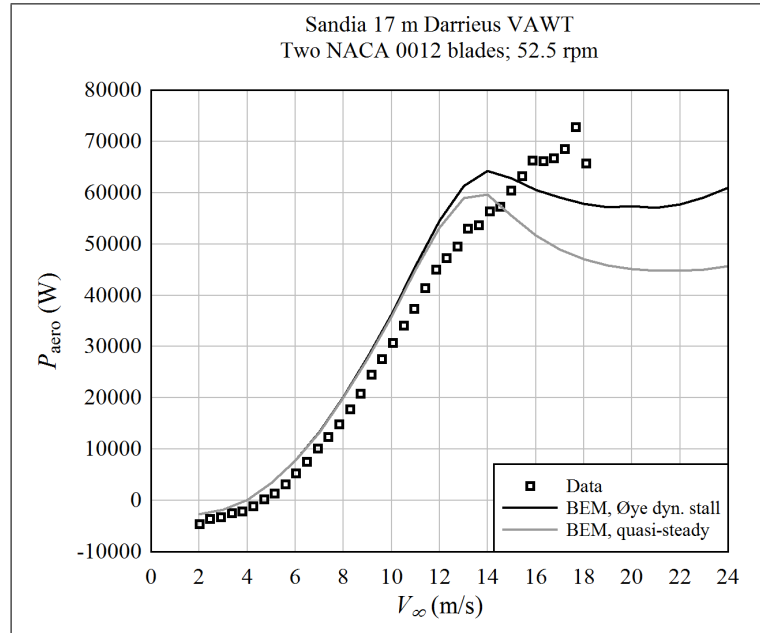


Figure 4.8: Aerodynamic power versus windspeed for the Sandia 17 m diameter turbine; two NACA 0012 blades; 52.5 rpm

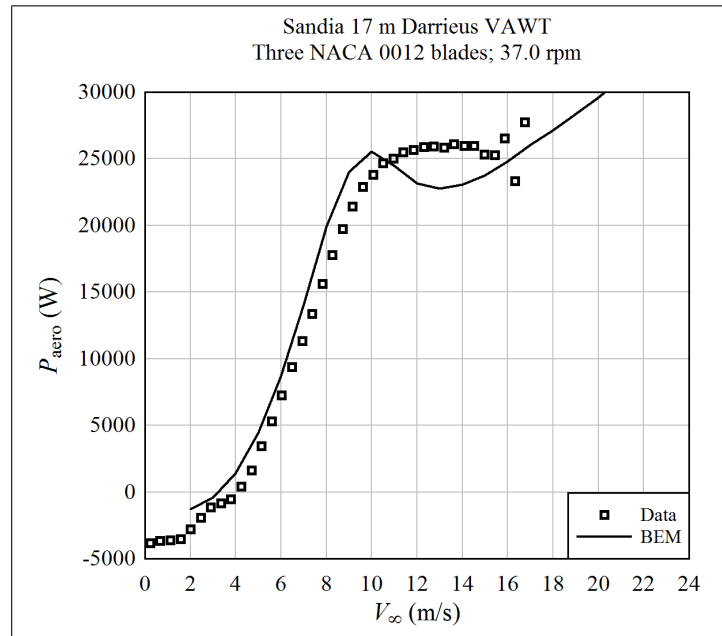


Figure 4.9: Aerodynamic power versus windspeed for the Sandia 17 m diameter turbine; three NACA 0012 blades; 37.0 rpm

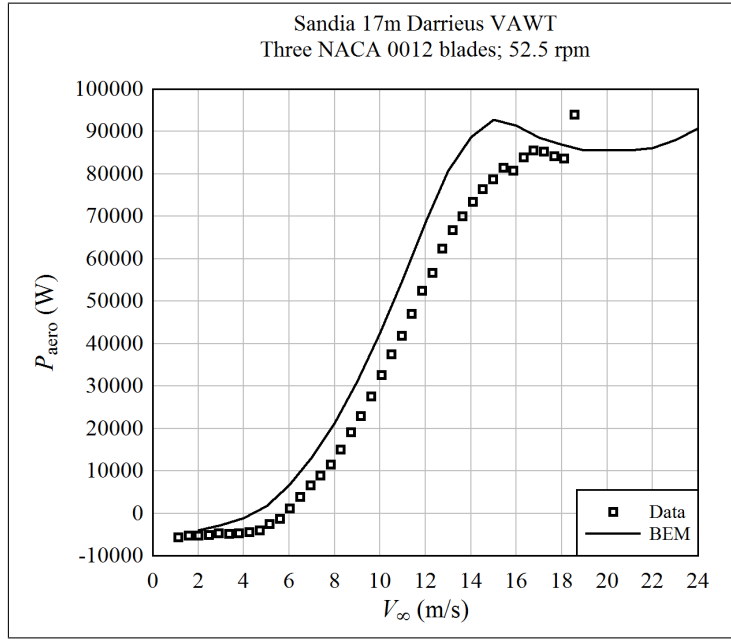


Figure 4.10: Aerodynamic power versus windspeed for the Sandia 17 m diameter turbine; three NACA 0012 blades; 52.5 rpm

Deepwind 5 MW design uses NACA 0018 airfoils, for which reliable coefficient data was not available. Lift coefficient data was taken from Jacobs and Sherman [9], but the drag data from this reference is not reliable. Therefore, drag was estimated based upon an empirical model in the author's thesis. [17]

The predicted power curves are shown in Figure 4.11. It appears that the analytical results in the design document were obtained without including dynamic stall. The difference between the two curves which do not include dynamic stall can likely be attributed to the airfoil coefficients.

Figure 4.12 compares the thrust curves. The results using quasi-steady coefficients compare well with the Deepwind reference values.



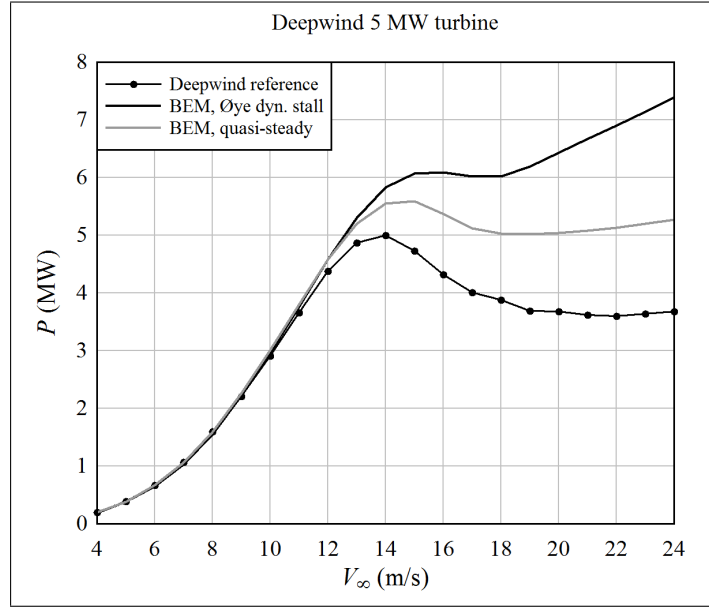


Figure 4.11: Average aerodynamic power versus windspeed for the Deepwind 5 MW preliminary design, compared against analytical results in the informal document describing the design

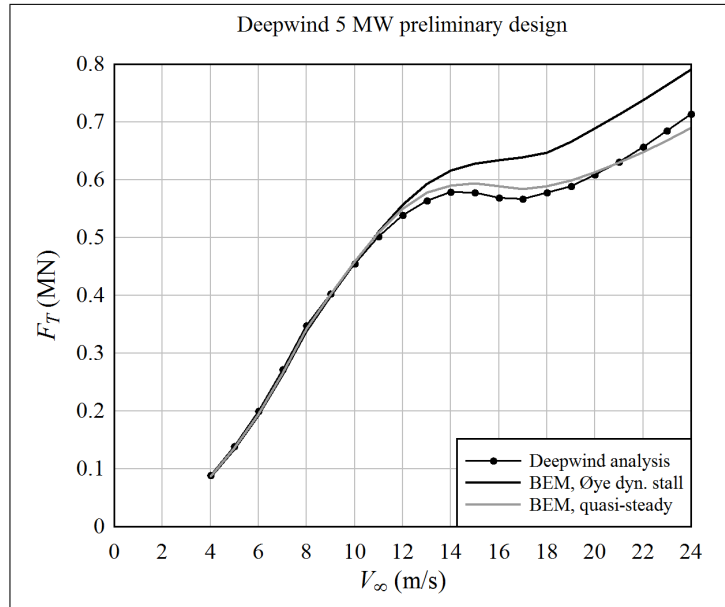


Figure 4.12: Average thrust versus windspeed for the Deepwind 5 MW preliminary design, compared against analytical results in the informal document describing the design

## Chapter 5

# Conclusions

A double-multiple streamtube BEM method has been programmed. The method provides aerodynamic loads on the blades of a VAWT, under conditions in which windspeeds fluctuate. The software is suitable for modelling the behavior of a VAWT in the presence of atmospheric turbulence, wakes from upwind turbines, or motion of the support platform.

The double-multiple streamtube BEM method is accurate when flow on the blades is attached, below the rated windspeed. Above the rated windspeed, when the blades are stalled, predictions of power output are poor. For more accurate estimates, it is necessary to calibrate the aerodynamic properties of the airfoils empirically; this is especially so for the model of dynamic stall.

The BEM method implemented here explicitly models many blades about the rotor azimuth, most of which are fictitious. Using such “ghost” blades allows the induced velocity, associated with each element on the swept surface, to respond smoothly to fluctuations in the local windspeed. The induced velocity and loads on the blades evolve naturally according to dynamic stall and dynamic inflow models.

The BEM method may be used for preliminary aerodynamic and structural design of a VAWT rotor. For detail design and certification, it is recommended to implement a more robust aerodynamic model.



# Bibliography

- [1] Abbott, I.H.; von Doenhoff, A.E.; *Theory of Wing Sections, Including a Summary of Airfoil Data*; Dover Publications, New York, USA, 1959
- [2] Burton, T., et al.; *Wind Energy Handbook*; John Wiley & Sons, UK, 2001
- [3] Fuglsang, P., et al.; “Wind Tunnel Test of the Risø-1 Airfoil”; Report Risø-R-999(EN), Risø National Laboratory, Roskilde, Denmark, 1998
- [4] Goett, H.J.; Bullivant, W.K.; “Tests of N.A.C.A. 009, 0012, and 0018 Airfoils in the Full-Scale Tunnel”; Report No. 647, National Advisory Committee for Aeronautics, USA, 1938
- [5] Gupta, S.; Leishman, J.G.; “Dynamic Stall Modelling of the S809 Aerofoil and Comparison with Experiments”; *Wind Energy* 9 (2006) 521-547
- [6] Hansen, M.H., et al.; “A Beddoes-Leishman Type Dynamic Stall Model in State-Space and Indicial Formulations”; Risø National Laboratory Report Risø-R-1354, Roskilde, Denmark, 2004
- [7] Hansen, M.O.L.; *Aerodynamics of Wind Turbines*; Second Edition, Earthscan, London, UK, 2008
- [8] Homicz, G.F.; “Numerical Simulation of VAWT Stochastic Aerodynamic Loads Produced by Atmospheric Turbulence: VAWT-SAL Code”; Report SAND91-1124, Sandia National Laboratories, Albuquerque, NM, USA, 1991
- [9] Jacobs, E.N.; Sherman, A.; “Airfoil Section Characteristics as Affected by Variations of the Reynolds Number”; Report No. 586, National Advisory Committee for Aeronautics, USA, 1937
- [10] Jacobs, E.N.; Abbott, I.H.; “Airfoil Section Data Obtained in the N.A.C.A. Variable-Density Tunnel as Affected by Support Interference and Other Corrections”; Report No. 669, National Advisory Committee for Aeronautics, USA, 1939
- [11] Larsen J.W.; Nielsen S.R.K.; Krenk S.; “Dynamic Stall Model for Wind Turbine Airfoils”; *Journal of Fluids and Structures* 23 (2007) 959-982
- [12] Leishman, J.G.; “Challenges in Modelling the Unsteady Aerodynamics of Wind Turbines”; *Wind Energy* 5 (2002) 85-132

- [13] Leishman, J.G.; Beddoes, T.S.; “A Generalised Model for Airfoil Unsteady Aerodynamic Behaviour and Dynamic Stall Using the Indicial Method”; Proceedings of the 42nd Annual Forum of the American Helicopter Society, Washington, D.C., June 1986, 243-265
- [14] Leishman, J.G.; Beddoes, T.S.; “A Semi-Empirical Model for Dynamic Stall”; Journal of the American Helicopter Society 34 (1989) 3-17
- [15] Lindenburg, C.; “Investigation into Rotor Blade Aerodynamics – Analysis of the stationary measurements on the UAE phase-VI rotor in the NASA-Ames wind tunnel”; Report ECN-C-03-025, Energy Research Centre of the Netherlands, 2003
- [16] Merz, K.O.; “BA8607 Final Project: Preliminary Concepts and Aerodynamic Analysis Methods for a Vertical-Axis Deepwater Offshore Wind Turbine”; Norwegian University of Science and Technology (NTNU), Department of Civil and Transport Engineering, Trondheim, Norway, 2009
- [17] Merz, K.O.; *Conceptual Design of a Stall-Regulated Rotor for a Deepwater Offshore Wind Turbine*; Doctoral Thesis 2011:191, Department of Civil Engineering, Norwegian University of Science and Technology, 2011
- [18] Merz, K.O.; “A Method for Analysis of VAWT Aerodynamic Loads under Turbulent Wind and Platform Motion”; to be presented at the 9th Deep Sea Offshore Wind R&D Seminar, Trondheim, Norway, January 19-20, 2012
- [19] Moriarty, P.J.; Hansen, A.C.; “Aerodyn Theory Manual”; Report NREL/TP-500-36881, National Renewable Energy Laboratory, Golden, CO, USA, 2005
- [20] Øye, S.; “Dynamic Stall, Simulated as a Time Lag of Separation”; McAnulty, K.F. (editor); Proceedings of the Fourth IEA Symposium on the Aerodynamics of Wind Turbines, ETSU-N-118, 1991
- [21] Paraschivoiu, I.; *Wind Turbine Design, with Emphasis on Darrieus Concept*; Polytechnic International Press, Montréal, Québec, Canada, 2002
- [22] Prandtl, L. (translated by the staff of the National Advisory Committee for Aeronautics); “Applications of Modern Hydrodynamics to Aeronautics”; NACA Report 116, USA, 1921
- [23] Sheldahl, R.E.; Klimas, P.C.; “Aerodynamic Characteristics of Seven Symmetrical Airfoil Sections Through 180-Degree Angle of Attack for Use in Aerodynamic Analysis of Vertical Axis Wind Turbines”; Report SAND80-2114, Sandia National Laboratories, Albuquerque, NM, USA, 1981
- [24] Snel, H.; Schepers, J.G.; “Joint Investigation of Dynamic Inflow Effects and Implementation of an Engineering Method”; ECN Report ECN-C-94-107, Energy Research Centre of the Netherlands, 1995
- [25] Wilson, R.E.; Lissaman, P.B.S.; “Applied Aerodynamics of Wind Power Machines”; Oregon State University, USA, 1974

- [26] Worstell, M.H.; “Aerodynamic Performance of the 17 Meter Diameter Darrieus Wind Turbine”; Report SAND78-1737, Sandia National Laboratories, Albuquerque, NM, USA, 1978
- [27] Worstell, M.H.; “Aerodynamic Performance of the 17-M-Diameter Darrieus Wind Turbine in the Three-Bladed Configuration: An Addendum”; Report SAND79-1753, Sandia National Laboratories, Albuquerque, NM, USA, 1979